



## King's Research Portal

DOI:

[10.1038/s41563-020-0783-8](https://doi.org/10.1038/s41563-020-0783-8)

*Document Version*

Peer reviewed version

[Link to publication record in King's Research Portal](#)

*Citation for published version (APA):*

Jowett, G. M., Norman, M. D. A., Yu, T. T. L., Rosell Arévalo, P., Hoogland, D., Lust, S. T., Read, E., Hamrud, E., Walters, N. J., Niazi, U., Chung, M. W. H., Marciano, D., Omer, O. S., Zabinski, T., Danovi, D., Lord, G. M., Hilborn, J., Evans, N. D., Dreiss, C. A., ... Gentleman, E. (2021). ILC1 drive intestinal epithelial and matrix remodelling. *NATURE MATERIALS*, 20(2), 250-259. <https://doi.org/10.1038/s41563-020-0783-8>

### **Citing this paper**

Please note that where the full-text provided on King's Research Portal is the Author Accepted Manuscript or Post-Print version this may differ from the final Published version. If citing, it is advised that you check and use the publisher's definitive version for pagination, volume/issue, and date of publication details. And where the final published version is provided on the Research Portal, if citing you are again advised to check the publisher's website for any subsequent corrections.

### **General rights**

Copyright and moral rights for the publications made accessible in the Research Portal are retained by the authors and/or other copyright owners and it is a condition of accessing publications that users recognize and abide by the legal requirements associated with these rights.

- Users may download and print one copy of any publication from the Research Portal for the purpose of private study or research.
- You may not further distribute the material or use it for any profit-making activity or commercial gain
- You may freely distribute the URL identifying the publication in the Research Portal

### **Take down policy**

If you believe that this document breaches copyright please contact [librarypure@kcl.ac.uk](mailto:librarypure@kcl.ac.uk) providing details, and we will remove access to the work immediately and investigate your claim.

## ILC1 drive intestinal epithelial and matrix remodelling

Geraldine M. Jowett<sup>1,2,3,4</sup>, Michael D. A. Norman<sup>\*1</sup>, Tracy T. L. Yu<sup>\*1</sup>, Patricia Rosell Arévalo<sup>2</sup>, Dominique Hoogland<sup>5</sup>, Suzette Lust<sup>1</sup>, Emily Read<sup>2,3</sup>, Eva Hamrud<sup>1,3,4</sup>, Nick J. Walters<sup>6</sup>, Umar Niazi<sup>7</sup>, Matthew Wai Heng Chung<sup>2,3,4</sup>, Daniele Marciano<sup>1</sup>, Omer Serhan Omer<sup>8,9</sup>, Tomasz Zabinski<sup>2</sup>, Davide Danovi<sup>4</sup>, Graham M. Lord<sup>10</sup>, Jöns Hilborn<sup>11</sup>, Nicholas D. Evans<sup>12</sup>, Cécile A. Dreiss<sup>13</sup>, Laurent Bozec<sup>14</sup>, Oommen P. Oommen<sup>15</sup>, Christian D. Lorenz<sup>16</sup>, Ricardo M.P. da Silva<sup>1,17</sup>, Joana F. Neves<sup>†#2</sup>, Eileen Gentleman<sup>†#1</sup>

<sup>1</sup> Centre for Craniofacial and Regenerative Biology, King's College London, London SE1 9RT, UK

<sup>2</sup> Centre for Host Microbiome Interactions, King's College London, London, SE1 9RT, UK

<sup>3</sup> Wellcome Trust Cell Therapies and Regenerative Medicine PhD programme

<sup>4</sup> Centre for Stem Cells & Regenerative Medicine, King's College London, London, SE1 9RT, UK

<sup>5</sup> Department of Chemistry, King's College London, London SE1 1DB, UK

<sup>6</sup> BioMediTech, Tampere University, 33014 Tampereen yliopisto, Finland, and Natural Resources Institute Finland, 00790 Helsinki, Finland

<sup>7</sup> Guy's and St Thomas' National Health Service Foundation Trust and King's College London National Institute for Health Research Biomedical Research Centre Translational Bioinformatics Platform, Guy's Hospital, London, UK

<sup>8</sup> School of Immunology and Microbial Sciences, King's College London, London, UK

<sup>9</sup> Department of Gastroenterology, Guy's and St Thomas' Hospitals NHS Trust, London, UK

<sup>10</sup> Faculty of Biology, Medicine and Health, University of Manchester, M13 9NT, UK

<sup>11</sup> Department of Chemistry, Ångström Laboratory, Uppsala University, Uppsala 75121, Sweden

<sup>12</sup> Bone and Joint Research Group, Centre for Human Development, Stem Cells and Regeneration, Human Development and Health, Institute of Developmental Sciences, University of Southampton, Southampton, UK.

<sup>13</sup> Institute of Pharmaceutical Science, Franklin-Wilkins Building, King's College London, London SE1 9NH, UK

<sup>14</sup> Faculty of Dentistry, University of Toronto, Toronto, Canada

<sup>15</sup> Bioengineering and Nanomedicine Lab, Faculty of Medicine and Health Technology, Tampere University, 33720 Tampere, Finland

<sup>16</sup> Department of Physics, King's College London, London WC2R 2LS, UK

<sup>17</sup> i3S - Instituto de Investigação e Inovação em Saúde and INEB - Instituto de Engenharia Biomédica, Universidade do Porto, Rua Alfredo Allen, 208, 4200 - 135 Porto, Portugal

\*These two authors contributed equally; listed in alphabetical order.

#These two authors contributed equally.

†To whom correspondence should be addressed: eileen.gentleman@kcl.ac.uk or joana.pereira\_das\_neves@kcl.ac.uk

Keywords: Hydrogel, Innate lymphoid cell, intestinal organoid, matrix remodelling, TGFβ1, CD44v6

41  
42  
43  
44  
45  
46  
47  
48  
49  
50  
51  
52  
53  
54  
55  
56  
57  
58  
59  
60  
61  
62  
63  
64  
65  
66  
67  
68  
69  
70  
71  
72  
73

**Abstract**

Organoids can shed light on the dynamic interplay between complex tissues and rare cell types within a controlled microenvironment. Here, we developed gut organoid co-cultures with type-1 innate lymphoid cells (ILC1) to dissect the impact of their accumulation in inflamed intestines. We demonstrate that murine and human ILC1 secrete TGFβ1, driving expansion of CD44v6<sup>+</sup> epithelial crypts. ILC1 additionally express MMP9 and drive gene signatures indicative of extracellular matrix remodelling. We therefore encapsulated human epithelial-mesenchymal intestinal organoids in MMP-sensitive, synthetic hydrogels designed to form efficient networks at low polymer concentrations. Harnessing this defined system, we demonstrate that ILC1 drive matrix softening and stiffening, which we suggest occurs through balanced matrix degradation and deposition. Our platform enabled us to elucidate previously undescribed interactions between ILC1 and their microenvironment, which suggest that they may exacerbate fibrosis and tumour growth when enriched in inflamed patient tissues.

74 **Main**

75

76 Intestinal epithelial cells (IEC)<sup>1</sup> interact with innate lymphoid cells (ILC)<sup>2</sup> to form a dynamic  
77 barrier between organisms and their environment. Together, they are capable of rapidly  
78 responding to danger and damage in an antigen non-specific manner. For instance, type-3 ILC  
79 secrete Interleukin-22 (IL-22, *Il22*) in response to extracellular pathogens, which promotes anti-  
80 microbial peptide secretion and proliferation of Lgr5<sup>+</sup> CD44<sup>+</sup> intestinal stem cells<sup>3</sup>. Conversely,  
81 type-1 ILC express Interferon-gamma (IFN $\gamma$ , *Ifng*) in response to intracellular pathogens, and  
82 are comprised of circulating natural killer (NK) cells and tissue resident helper-like ILC1 (ILC1),  
83 which are considered less cytotoxic than their NK-cell counterparts<sup>4</sup>. Notably, ILC1 accumulate  
84 in the inflamed intestines of Inflammatory Bowel Disease (IBD) patients<sup>5</sup>, however the nature of  
85 their subset-specific interactions with the epithelium has remained elusive. Understanding the  
86 impact of ILC1 enrichment could inform on alternative strategies for treating this complex  
87 disease, which is a pressing issue as only a third of patients respond to gold standard TNF $\alpha$ -  
88 blocking biologics<sup>6</sup>.

89

90 Teasing apart the role of rare cell populations in multifactorial diseases is challenging, and  
91 redundant cytokine signalling pathways *in vivo* can obscure ILC-specific phenotypes. Thus, to  
92 explore the impact of ILC1 on IEC we developed a reductionist co-culture system with murine  
93 small intestine organoids (SIO)<sup>7</sup>. We unexpectedly found that ILC1-derived TGF $\beta$ 1 induces  
94 p38 $\gamma$  phosphorylation, driving proliferation of CD44v6<sup>+</sup> epithelial cells. Moreover, pathway  
95 analysis of co-culture transcriptomes predicted ILC1-driven matrisome remodelling, so we  
96 developed highly defined PEG-based hydrogels to quantitatively characterize the impact of ILC1  
97 on matrix remodelling in a human iPSC-derived organoid model (HIO)<sup>8</sup>. We not only confirmed  
98 that IBD patient-derived ILC1 express *TGFB1* to upregulate intestinal CD44v6, but also that  
99 they prompt physical changes in the hydrogel via both degradation and production of peri-  
100 organoid matrix. Our findings suggest an unexpected role for ILC1 in intestinal remodelling,  
101 which could exacerbate IBD-associated comorbidities when enriched in inflamed intestines.

102

103

104

105

106

107

108 **Results**

109

110 **ILC1 drive CD44<sup>+</sup> crypt expansion**

111

112 To study the impact of ILC1 accumulation on IEC, we established co-cultures of murine SIO and  
113 small intestinal lamina propria-derived ILC1 (Fig. 1a-c and Supplementary Figure 1). ILC1  
114 maintained characteristic KLRG1<sup>-</sup>, RORγt<sup>+</sup>, NK1.1<sup>+</sup> expression after co-culture (Supplementary  
115 Figure 2, 3a), and expressed *Ifng*, but not *Ii22*, matching freshly isolated ILC1 (Fig. 1d). We  
116 tuned this system to contain low-levels of IFNγ secretion (Supplementary Figure 3b,c), and  
117 cultured SIO either alone or with ILC1 for 4 days. We then FACS-purified IEC for bulk Smart-  
118 seq2 pico-RNAsequencing. ILC1 co-culture significantly increased expression of epithelial  
119 *Cd44*, a common crypt stem cell marker that can act as a growth factor co-receptor, a  
120 transcription factor, or mediate cell surface adhesion<sup>9</sup> (Fig. 1e, Supplementary Figure 2, and  
121 Supplementary Data Set 1). ILC1 also promoted the growth of enlarged CD44<sup>+</sup> crypt buds (Fig.  
122 1f-h). To explore whether IFNγ drove this effect, we supplemented SIO-only cultures with  
123 recombinant IFNγ, which did not increase epithelial proliferation or *Cd44* expression (Fig. 1i, j).  
124 Moreover, Ingenuity Pathway Analysis (IPA) of the SmartSeq2 dataset did not predict *IFNG* as a  
125 dominant signature of ILC1 co-culture (Fig. 1k), suggesting that ILC1 upregulate CD44 through  
126 an alternate mechanism.

127

128 **ILC1 secrete TGFβ1**

129

130 As predicted by the IPA upstream regulators, we detected increased levels of TGFβ1 in the  
131 ILC1 co-culture supernatants (Fig. 2a). Stimulated ILC1 expressed *Tgfb1* before and after co-  
132 culture (Fig. 2b), mimicking expression patterns of *Ifng* (Fig. 1d). Although epithelial cells can  
133 express *Tgfb1* in response to microbiome metabolites<sup>10</sup>, IEC expression of *Tgfb1* was negligible  
134 both with and without ILC1 co-culture (Fig. 2c). However, SIO in our system maintained  
135 expression of TGFβR1 (Fig. 2d), and broadly upregulated this receptor across the entire  
136 epithelium in ILC1 co-cultures (Supplementary Figure 4), indicating that SIO retained the  
137 capacity to respond to exogenous TGFβ1.

138

139 We next investigated whether TGFβ1 accounted for CD44 upregulation. First, we established  
140 that the phenotype was not contact dependent (Supplementary Figure 5). We then distinguished  
141 between common splice isoforms of CD44 using intron-specific primers<sup>11</sup> and found that ILC1

142 co-culture upregulated CD44 variant 6 (*Cd44v6*) specifically, which was inhibited by TGFβ<sub>1,2,3</sub>  
143 neutralizing antibody and upregulated by recombinant TGFβ<sub>1</sub> in SIO-only cultures (Fig. 2e).  
144 Importantly, TGFβ<sub>1,2,3</sub> inhibition did not adversely impact ILC1 viability or phenotype  
145 (Supplementary Figure 6). CD44v6 protein was ubiquitously distributed across the basolateral  
146 membrane of the SIO crypt in co-cultures (Fig. 2f), and did not appear to concentrate in specific  
147 IEC subsets. TGFβ<sub>1</sub>-induced expression of CD44v6 has been described in fibrotic lung  
148 fibroblasts<sup>12</sup>, however this is to our knowledge the first description of such a connection in the  
149 intestinal epithelium.

150  
151 CD44 engages in a positive feedback loop with Wnt/β-catenin. Indeed, it is a downstream target  
152 of β-catenin, and clusters with Lrp6 to potentiate Wnt signalling<sup>13</sup>. Moreover, IPA predicted  
153 significant increases in both p38/MAPK and Wnt/β-catenin signalling in SIO co-cultured with  
154 ILC1 (Fig. 2g). We observed accumulation of epithelial β-catenin in ILC1 co-cultures (Fig. 2h),  
155 and increased expression of β-catenin-targets *Ascl2* and *Axin2* (Supplementary Figure 7a). β-  
156 catenin accumulation co-localized with CD44v6<sup>+</sup> expression (Supplementary Figure 7b), and  
157 was reversible by TGFβ<sub>1,2,3</sub> neutralization (Fig. 2i). We first hypothesized that increased crypt  
158 size in ILC1 co-cultures could be driven by CD44/β-catenin induced modulation of IEC  
159 differentiation, however despite a trending bias toward expression of stem cell crypt over mature  
160 enterocyte markers, differences in subset-specific genes were not statistically significant  
161 (Supplementary Figure 8). Instead, IEC that upregulated CD44v6 and β-catenin also showed a  
162 dramatic increase in phosphorylated p38 signal (Fig. 2h), which was equally upregulated by  
163 ILC1 co-culture and downregulated through TGFβ<sub>1,2,3</sub> neutralization (Fig. 2j). This kinase  
164 exists in multiple isoforms, and while p38α/β regulates apoptosis, p38γ promotes proliferation.  
165 To investigate which isoform was active in our co-cultures, we used p38α/β-inhibitor PD169316  
166 (PD16) and p38γ-inhibitor Pirfenidone, a drug approved for the treatment of pulmonary  
167 fibrosis<sup>14</sup>. These soluble inhibitors impacted ILC1 phenotypes (Supplementary Figure 9a), so we  
168 mimicked ILC1 co-culture through addition of recombinant TGFβ<sub>1</sub>. SIO cultured with  
169 Pirfenidone, but not PD16, significantly and specifically downregulated *Cd44v6* (Fig. 2k,  
170 Supplementary Figure 9b) and *Axin2* (Fig. 2l), and reversed crypt budding, as did TGFβ<sub>1,2,3</sub>  
171 neutralization (Fig. 2m). It is reported that p38γ phosphorylates the Ser605 residue of β-catenin,  
172 thus stabilizing this mitogenic transcription factor, and driving inflammation-associated intestinal  
173 tumourigenesis<sup>15</sup>. This suggests that p38γ activity likely acts downstream of TGFβ<sub>1</sub> and  
174 upstream of β-catenin and CD44v6 upregulation in our co-cultures, which could promote IEC

175 subtype non-specific proliferation and organoid growth through a positive CD44v6/ $\beta$ -catenin  
176 feedback loop.

177

178

### 179 **IBD-patient ILC1 upregulate intestinal CD44v6**

180

181 Next, we isolated human intestinal lamina propria ILC1 (hILC1) from IBD patient biopsies  
182 (Supplementary Figure 10), and established co-cultures with human gut organoids  
183 (Supplementary Figure 11, 12). Epithelial-only biopsy-derived enteroids<sup>16</sup> closely mimic SIO, but  
184 as these maintain epigenetic signatures of their donors<sup>17</sup>, they offer no control over patients'  
185 genetic background or exposure to environmental stressors, diet, or drugs. Conversely,  
186 differentiation<sup>18</sup> and maturation<sup>19</sup> of human iPSC-derived intestinal organoids (HIO) provides  
187 greater control over genetics and environment, which are necessary for modelling multifactorial  
188 diseases. Following 7-day co-culture with HIO, hILC1 maintained their phenotypic response to  
189 activation, upregulating *IFNG* but not *IL22* (Fig. 3a). In this system, hILC1 co-culture increased  
190 basolateral CD44v6 expression in HIO-IEC (Fig. 3b), which was recapitulated through addition  
191 of recombinant TGF $\beta$ 1 (Supplementary Figure 13). Strikingly, the increase in *CD44v6*  
192 expression was only statistically significant when hILC1 were derived from sites of active  
193 inflammation (Fig. 3c), which yielded more ILC1, recapitulating the previously reported<sup>5</sup>  
194 accumulation of this ILC subset (Fig. 3d, Supplementary Figure 10). Intriguingly, hILC1 from  
195 inflamed tissues also proliferated more in co-culture than those from uninfamed biopsies (Fig.  
196 3e). This suggests that the inflamed IBD microenvironment left a proliferative imprint on hILC1,  
197 which was maintained *ex vivo* in a reductionist system with constant intestinal genetics, cytokine  
198 exposure, environmental stimuli, and microbiome composition. However, hILC1 from both  
199 conditions expressed *TGFB1* before (Supplementary Figure 14) and after co-culture with HIO  
200 (Fig. 3f), and expression levels did not differ significantly between cultures from inflamed and  
201 uninfamed tissues. We therefore suggest that the differential upregulation of *CD44v6* in  
202 inflamed co-cultures resulted from the increased number of hILC1 in this system, not due to cell-  
203 intrinsic differences in *TGFB1* expression. Thus, hILC1 from inflamed IBD patients provide a  
204 disease-relevant *in vitro* model of the impact of hILC1 accumulation on the gut, allowing us to  
205 appropriately explore murine co-culture data in a translationally relevant system.

206

207 To confirm this clinical relevance of data obtained in this system, we performed  
208 immunohistochemistry on inflamed and uninfamed intestinal biopsies. We observed an

209 increase in epithelial CD44v6 expression along the basolateral junctions of enlarged crypts in  
210 inflamed tissues. This underscored that co-cultures of SIO+ILC1 and HIO+hILC1 (from patients  
211 with active inflammation) both predicted and recapitulated CD44v6 upregulation in inflamed IBD  
212 tissues. However, we also noticed CD44v6 expression beyond the epithelial compartment in the  
213 inflamed sections, in both CD45<sup>+</sup> lymphocytes and in basal lamina fibroblasts (Fig. 3g). Since  
214 inflamed tissues are infiltrated by many different immune cells, we could not determine whether  
215 the apparent mesenchymal upregulation was related to hILC1 accumulation, and therefore  
216 returned to the HIO model. HIO co-develop with organized layers of mesenchymal fibroblasts,  
217 closely mimicking the ECM environment of the native intestine (Fig. 3h). We found that HIO  
218 fibroblasts expressed significantly more *CD44v6* after co-culture with hILC1 from inflamed  
219 tissues (Fig. 3i), suggesting a causal link between hILC1 and mesenchymal remodelling. Since  
220 TGFβ1 is a master regulator of fibrosis, and pathological matrix remodelling is a hallmark of  
221 IBD<sup>20</sup>, this merited further investigation.

222

### 223 **Synthetic hydrogels allow quantification of matrix remodelling**

224

225 The responsiveness of fibroblasts to hILC1 piqued our interest, as Gene Set Enrichment  
226 Analysis (GSEA) of the murine SIO dataset had revealed significant enrichment of ECM-  
227 remodelling genes in co-culture (Supplementary Figure 15). We also frequently observed  
228 degradation of Matrigel in murine ILC1 co-cultures, which was reversible through MMP-inhibition  
229 (Supplementary Figure 16a-d). Moreover, we found that murine and human ILC1 specifically  
230 express gelatinase MMP9, a biomarker for IBD<sup>21</sup> (Supplementary Figure 16e,f). Until this point,  
231 experiments were conducted by resuspending cultures in 3D mouse sarcoma-derived Matrigel.  
232 This laminin-rich gel could mask or modulate matrix deposition by fibroblasts, and while it is  
233 degradable by native enzymes, the manufacturer adds proprietary concentrations of undefined  
234 MMP inhibitors<sup>22</sup>, precluding experiments that require precise control over and quantification of  
235 matrix remodelling.

236

237 To appropriately address this question, we required a highly defined 3D system with physical  
238 properties akin to the native intestine, but whose degradability could be independently  
239 modulated. PEG-based hydrogels with suitable stiffness have been reported, but require cross-  
240 linking by transglutaminase Factor XIIIa<sup>23</sup> which is known to crosslink ECM components like  
241 fibronectin. Fully synthetic hydrogels in which homo-bifunctional peptides (A<sub>2</sub>) act as  
242 crosslinkers of 4- or 8-arm PEGs (B<sub>4</sub>/B<sub>8</sub>) have also been described; however, when crosslinkers



243 bear two identical functional groups that react indiscriminately towards the chain-end of any  
244 PEG arm, primary ( $1^\circ$ ) loop formation<sup>24</sup> can impact network connectivity. This is critical when  
245 forming soft, tissue-like hydrogels which require low polymer concentrations, resulting in slow  
246 and inefficient network formation in which organoids reach the tissue culture plastic beneath the  
247 hydrogel prior to 3D gelation<sup>25</sup>.

248  $A_4+B_4$  hydrogel designs that avoid  $1^\circ$  looping could yield more effectively cross-linked networks  
249 than  $A_2+B_4$  systems<sup>26</sup> (Fig. 4a). To explore if this held true at low polymer concentrations, we  
250 carried out molecular dynamics (MD) simulations, using a coarse grain approach. MD uses  
251 classical laws of mechanics to provide insight into probable molecular arrangements within a  
252 material. Simulations showed that  $A_4+B_4$  designs facilitated the formation of more network-  
253 forming cross-links than  $A_2+B_4$  designs in which  $\sim 25\%$  of cross-links were  $1^\circ$  loops (Fig. 4b and  
254 Supplementary Figs. 17 and 18).

255 To create an  $A_4+B_4$  design, we formed hydrogels using two sequential click reactions in which  
256 all peptides acted as cross-linkers (Fig. 4c and Supplementary Figure 19). First, an amine at  
257 peptides' N-terminal was reacted with PEG-4NPC ( $A_4$ ), yielding PEG-peptide conjugates  
258 (conjugation efficiency 81-91%). Hydrogels were then formed through a Michael addition  
259 between a C-terminal free thiol on the unconjugated peptide arm with the end-terminus of PEG-  
260 4VS ( $B_4$ ) (>90% efficiency) (Supplementary Figure 20).  $A_4+B_4$  hydrogels had more effectively  
261 cross-linked networks with lower swelling ratios (Fig. 4d) that were both stiffer and behaved  
262 more elastically (Fig. 4e and Supplementary Figure 21) than  $A_2+B_4$  designs formed using homo-  
263 bifunctional peptides. Moreover, although  $A_4+B_4$  hydrogels abandoned standard pendant  
264 presentations of adhesive ligands, human mesenchymal stromal cells could still adhere to their  
265 surfaces (Supplementary Figure 22).  $A_4+B_4$  hydrogels' Young's modulus ( $E$ ) could be varied by  
266 modulating polymer concentration (Fig. 4f) to achieve values for  $E$  similar to that of normal  
267 human intestinal tissue ( $750-1250\text{Pa}$ )<sup>27</sup>, and were susceptible to degradation by MMP9 (Fig.  
268 4g). Taken together, this suggests suitable properties to explore HIO matrix remodelling.

269

## 270 **Human ILC1 drive matrix remodelling**

271

272 Equipped with an appropriate culture system, we found that HIO encapsulated in degradable,  
273 non-degradable, and intermediately degradable (IM-DEG, 45% MMP-cleavable peptides)  
274 hydrogels were viable (Fig. 4h, Supplementary Figure 23), and maintained their characteristic  
275 phenotype, as in Matrigel (Fig. 4 i,j; Supplementary Figure 24a,b). Moreover, HIO fibroblasts

276 were capable of depositing native extracellular matrix in this system, which also did not alter  
277 CD44 expression (Supplementary Figure 25b,c,d). We then harnessed this system to  
278 quantitatively dissect the impact of hILC1 on the physical properties of HIO-hydrogel cultures.

279

280 First, we used atomic force microscopy (AFM)-based indentation to map cell-mediated changes  
281 in stiffness. Since phenotypically irrelevant differences in mechanical properties between  
282 conditions could come from the physical presence of hILC1 within the gel, we opted to surround  
283 the HIO-laden hydrogels with ancillary hILC1 from inflamed biopsies (aILC1), keeping the  
284 composition of the microenvironment that we mapped constant (Fig. 5a). We collected force-  
285 distance measurements using a bead-functionalized cantilever (Supplementary Figure 26), and  
286 observed increased heterogeneity of  $E$  across maps with aILC1 (Fig. 5b). Indeed, we saw a  
287 significant difference in variance of  $E$  induced by co-culture with aILC1 ( $F=0.0004$ ;  $p_{\chi^2}$   
288  $=0.0011$ )(Fig. 5c). Since aILC1 appeared to induce both stiffening and softening of the matrix,  
289 while median  $E$  remained comparable between samples, this could suggest a balance between  
290 cell-mediated matrix production and degradation.

291

292 To ensure that aILC1 had the same capacity to degrade engineered hydrogels as Matrigel, we  
293 next performed multiple particle tracking microrheology, monitoring the Brownian motion of  
294 fluorescent fiducial beads distributed within the hydrogel (Fig. 5d). Beads are capable of moving  
295 within degradable hydrogels (100% MMP-cleavable peptides) when enzyme-mediated  
296 degradation causes a sufficient portion of their local environment to undergo a gel-sol transition,  
297 prompting the logarithmic slope of a bead's mean-squared displacement,  $\alpha$ , to transition from 0  
298 to  $1^{28}$  (Fig. 5e). After 7 days, aILC1 co-culture significantly increased  $\alpha$  relative to HIO-only  
299 controls (Fig. 5f), with near complete degradation after 2 weeks ( $\alpha=0.847$ ). While the 55% non-  
300 degradable IM-DEG gel used for AFM was explicitly designed to not undergo a gel-sol  
301 transition, this microrheological quantification of aILC1's capacity to degrade a 100% MMP-  
302 sensitive system provides explanation for the softening recorded by AFM, which is sensitive to  
303 subtle changes in the stiffness of  $\sim 1$ kPa hydrogels.

304

305 Next, we assessed how ILC1 might contribute to hydrogel stiffening observed in fibroblast-rich,  
306 peri-organoid regions. We observed that aILC1 drove a significant increase in the area of peri-  
307 organoid FN1 deposition (Fig. 5g, Supplementary Figure 27). This phenotype was recapitulated  
308 in Matrigel, where aILC1 increased expression of *FN1* and *COL1a1* in HIO-fibroblasts (Fig. 5h,  
309 Supplementary Figure 28a), and increased FN1 deposition, which was recapitulated with

310 recombinant TGFβ1 (Supplementary Figure 28b). Specific upregulation of Fibronectin1 is  
311 consistent with non-canonical, SMAD-independent TGFβ1 signalling via Jun/p38, which drives  
312 *FN1* expression<sup>29</sup>. We therefore suggest that a balance between ILC1-derived MMP  
313 degradation and ILC1-induced mesenchymal ECM deposition account for the quantitative  
314 difference in coefficient of variance captured in the AFM stiffness maps. In summary, our A<sub>4</sub>+B<sub>4</sub>  
315 defined hydrogel allowed us to conclusively assess that hILC1 drive extracellular matrix  
316 remodelling in the intestine.

317

## 318 **Discussion**

319

320 Here, we identified murine ILC1 as an important source of TGFβ1, which promotes CD44v6<sup>+</sup>  
321 epithelial crypt growth through p38γ-induced proliferation (Fig. 6a). ILC1 isolated from IBD  
322 patients with active inflammation and recombinant TGFβ1 also drove upregulation of CD44v6 in  
323 epithelial and mesenchymal cells. To more thoroughly investigate this role of hILC1 in  
324 mesenchymal remodelling emerging from our data, we then developed a highly defined  
325 synthetic hydrogel system, which allowed us to quantify hILC1-mediated matrix degradation and  
326 stiffening. The introduction of TGFβ1 and MMP9 as a part of the ILC1 inflammatory response is  
327 in line with a recently published RNA-sequencing dataset of human ILC1, which showed  
328 increased expression of *TGFB1* and *MMP9* in patients with an acute risk of myocardial  
329 infarction relative to healthy controls<sup>30</sup>.

330

331 Speculation about the impact of TGFβ1 in the context of the gastro-intestinal immune system is  
332 a complex task, as the microbiome, the enteric nervous system, and other immune cells  
333 differentially respond to this pleiotropic cytokine. For instance, while TGFβ1 is a master  
334 regulator of fibrosis in fibroblasts<sup>31</sup>, it is anti-inflammatory in the adaptive immune system<sup>32</sup>, and  
335 can regulate plasticity between the ILC subsets<sup>33</sup>. We observed expression of TGFβ1 in tandem  
336 with IFNγ, suggesting that these cytokines may act in concert, and highlighting the importance  
337 of our dataset being derived from co-cultures with ILC1, not recombinant cytokines. Moreover,  
338 despite the presence of IFNγ in our system, pathway analysis predicted a decrease in  
339 inflammatory phenotypes, but an increase in epithelial gene signatures consistent with tumour  
340 growth and fibrosis (Fig. 6b). This fits with the pathogenic association of splice variant CD44v6,  
341 which exacerbates aggressive ovarian cancer by driving β-catenin expression<sup>34</sup>, driving  
342 intestinal cancer initiation<sup>35</sup>, progression<sup>9,36</sup>, and metastasis<sup>37</sup> in these tissues. Moreover, fibrotic  
343 Fibronectin deposition correlates with resistance to anti-TNFα treatment in Crohn's Disease

344 patients<sup>38</sup>. Thus, our findings suggest that while ILC1 may have an unexpected anti-  
345 inflammatory role in the gut, their accumulation in inflamed tissues could exacerbate IBD-  
346 associated comorbidities, and be an indicator for poor treatment response. This unexpected  
347 contextualization of intestinal ILC1 was enabled by our reductionist, modular, and synthetic  
348 culture system, which could be further exploited to dissect dynamic interactions between other  
349 inaccessible cells and tissues, in both development and disease.

350

351 **References**

- 352
- 353 1. Haber, A. L. *et al.* A single-cell survey of the small intestinal epithelium. *Nature* **551**, 333-339
- 354 (2017).
- 355 2. Vivier, E. *et al.* Innate Lymphoid Cells: 10 Years On. *Cell* **174**, 1054-1066 (2018).
- 356 3. Lindemans, C. *et al.* Interleukin-22 promotes intestinal-stem-cell-mediated epithelial
- 357 regeneration. *Nature* **528**, 560 (2015).
- 358 4. Spits, H., Bernink, J. H. & Lanier, L. NK cells and type 1 innate lymphoid cells: partners in
- 359 host defense. *Nature Immunology* **17**, 758-764 (2016).
- 360 5. Bernink, J. H. *et al.* Human type 1 innate lymphoid cells accumulate in inflamed mucosal
- 361 tissues. *Nature Immunology* **14**, 221-229 (2013).
- 362 6. Pagnini, C., Pizarro, T. T. & Cominelli, F. Novel Pharmacological Therapy in Inflammatory
- 363 Bowel Diseases: Beyond Anti-Tumor Necrosis Factor. *Front. Pharmacol.* **10** (2019).
- 364 7. Sato, T. *et al.* Paneth cells constitute the niche for Lgr5 stem cells in intestinal crypts. *Nature*
- 365 **469**, 415-418 (2011).
- 366 8. Spence, J. R. *et al.* Directed differentiation of human pluripotent stem cells into intestinal
- 367 tissue in vitro. *Nature* **470**, 105-9 (2011).
- 368 9. Senbanjo, L. T. & Chellaiah, M. A. CD44: A Multifunctional Cell Surface Adhesion Receptor Is
- 369 a Regulator of Progression and Metastasis of Cancer Cells. *Frontiers in cell and developmental*
- 370 *biology* **5**, 18 (2017).
- 371 10. Martin-Gallausiaux, C. *et al.* Butyrate produced by gut commensal bacteria activates TGF-
- 372 beta1 expression through the transcription factor SP1 in human intestinal epithelial cells.
- 373 *Scientific Reports* **8**, 1-13 (2018).
- 374 11. Zeilstra, J. *et al.* Stem cell CD44v isoforms promote intestinal cancer formation in Apc(min)
- 375 mice downstream of Wnt signaling. *Oncogene* **33**, 665-670 (2014).
- 376 12. Ghatak, S. *et al.* Transforming growth factor  $\beta$ 1 (TGF $\beta$ 1) regulates CD44V6 expression and
- 377 activity through extracellular signal-regulated kinase (ERK)-induced EGR1 in pulmonary
- 378 fibrogenic fibroblasts. *Journal of Biological Chemistry* **292**, 10465-10489 (2017).
- 379 13. Schmitt, M., Metzger, M., Gradl, D., Davidson, G. & Orian-Rousseau, V. CD44 functions in
- 380 Wnt signaling by regulating LRP6 localization and activation. *Cell death and differentiation* **22**,
- 381 677-689 (2015).
- 382 14. Ribes, B. M. *et al.* Effectiveness and safety of pirfenidone for idiopathic pulmonary fibrosis.
- 383 *Eur J Hosp Pharm* (2019).
- 384 15. Yin, N. *et al.* p38 $\gamma$  MAPK is required for inflammation-associated colon tumorigenesis.
- 385 *Oncogene* **35**, 1039-1048 (2016).
- 386 16. Fujii, M. *et al.* Human Intestinal Organoids Maintain Self-Renewal Capacity and Cellular
- 387 Diversity in Niche-Inspired Culture Condition. *Cell Stem Cell* **23**, 787-793.e6 (2018).
- 388 17. Dotti, I. *et al.* Alterations in the epithelial stem cell compartment could contribute to
- 389 permanent changes in the mucosa of patients with ulcerative colitis. *Gut* **66**, 2069-2079 (2017).
- 390 18. McCracken, K. W., Howell, J. C., Wells, J. M. & Spence, J. R. Generating human intestinal
- 391 tissue from pluripotent stem cells in vitro. *Nature Protocols* **6**, 1920-1928 (2011).
- 392 19. Jung, K. B. *et al.* Interleukin-2 induces the in vitro maturation of human pluripotent stem cell-
- 393 derived intestinal organoids. *Nature Communications* **9**, 1-13 (2018).
- 394 20. Shimshoni, E., Yablecovitch, D., Baram, L., Dotan, I. & Sagi, I. ECM remodelling in IBD:
- 395 innocent bystander or partner in crime? The emerging role of extracellular molecular events in
- 396 sustaining intestinal inflammation. *Gut* **64**, 367-372 (2015).
- 397 21. Farkas, K. *et al.* The Diagnostic Value of a New Fecal Marker, Matrix Metalloprotease-9, in
- 398 Different Types of Inflammatory Bowel Diseases. *Journal of Crohn's and Colitis* **9**, 231-237
- 399 (2015).
- 400 22. Hughes, C. S., Postovit, L. M. & Lajoie, G. A. Matrigel: A complex protein mixture required
- 401 for optimal growth of cell culture. *PROTEOMICS* **10**, 1886-1890 (2010).

- 402 23. Ehrbar, M. *et al.* Biomolecular Hydrogels Formed and Degraded via Site-Specific Enzymatic  
403 Reactions. *Biomacromolecules* **8**, 3000-3007 (2007).
- 404 24. Zhong, M., Wang, R., Kawamoto, K., Olsen, B. D. & Johnson, J. A. Quantifying the impact of  
405 molecular defects on polymer network elasticity. *Science (New York, N.Y.)* **353**, 1264-8 (2016).
- 406 25. Cruz-Acuña, R. *et al.* PEG-4MAL hydrogels for human organoid generation, culture, and in  
407 vivo delivery. *Nature Protocols* **13**, 2102-2119 (2018).
- 408 26. Gu, Y. *et al.* Semibatch monomer addition as a general method to tune and enhance the  
409 mechanics of polymer networks via loop-defect control. *Proceedings of the National Academy of  
410 Sciences of the United States of America* **114**, 4875-4880 (2017).
- 411 27. Stewart, D. C. *et al.* Quantitative assessment of intestinal stiffness and associations with  
412 fibrosis in human inflammatory bowel disease. *PLOS ONE* **13**, e0200377 (2018).
- 413 28. Schultz, K. M., Kyburz, K. A. & Anseth, K. S. Measuring dynamic cell-material interactions  
414 and remodeling during 3D human mesenchymal stem cell migration in hydrogels. *PNAS* **112**,  
415 E3757-E3764 (2015).
- 416 29. Hocevar, B. A., Brown, T. L. & Howe, P. H. TGF-beta induces fibronectin synthesis through  
417 a c-Jun N-terminal kinase-dependent, Smad4-independent pathway. *EMBO J.* **18**, 1345-1356  
418 (1999).
- 419 30. Li, J., Wu, J., Zhang, M. & Zheng, Y. Dynamic changes of innate lymphoid cells in acute ST-  
420 segment elevation myocardial infarction and its association with clinical outcomes. *Scientific  
421 Reports* **10**, 1-12 (2020).
- 422 31. Bauché, D. & Marie, J. C. Transforming growth factor  $\beta$ : a master regulator of the gut  
423 microbiota and immune cell interactions. *Clinical & Translational Immunology* **6**, e136 (2017).
- 424 32. Fenton, T. M. *et al.* Inflammatory cues enhance TGF $\beta$  activation by distinct subsets of  
425 human intestinal dendritic cells via integrin  $\alpha\beta 8$ . *Mucosal immunology* **10**, 624-634 (2017).
- 426 33. Bal, S. M., Golebski, K. & Spits, H. Plasticity of innate lymphoid cell subsets. *Nature  
427 Reviews Immunology*, 1-14 (2020).
- 428 34. Wang, J. *et al.* CD44v6 promotes  $\beta$ -catenin and TGF- $\beta$  expression, inducing aggression in  
429 ovarian cancer cells. *Mol Med Rep* **11**, 3505-3510 (2015).
- 430 35. Wang, Z., Zhao, K., Hackert, T. & Zöller, M. CD44/CD44v6 a Reliable Companion in  
431 Cancer-Initiating Cell Maintenance and Tumor Progression. *Frontiers in Cell and Developmental  
432 Biology* **6**, 97 (2018).
- 433 36. Ma, L., Dong, L. & Chang, P. CD44v6 engages in colorectal cancer progression. *Cell Death  
434 & Disease* **10**, 30 (2019).
- 435 37. Todaro, M. *et al.* CD44v6 Is a Marker of Constitutive and Reprogrammed Cancer Stem Cells  
436 Driving Colon Cancer Metastasis. *Cell Stem Cell* **14**, 342-356 (2014).
- 437 38. de Bruyn, J. R. *et al.* Intestinal fibrosis is associated with lack of response to Infliximab  
438 therapy in Crohn's disease. *PLoS One* **13** (2018).

439

440

441

442

443

444

445

446 Acknowledgements

447 G.M.J. acknowledges a Ph.D. fellowship from the Wellcome Trust (203757/Z/16/A) and a BRC  
448 Bright Sparks Precision Medicine Early Career Research Award. E.G. acknowledges a Philip  
449 Leverhulme Prize from the Leverhulme Trust. J.F.N. acknowledges a Marie Skłodowska-Curie  
450 Fellowship, a King's Prize fellowship, a RCUK/UKRI Rutherford Fund fellowship  
451 (MR/R024812/1) and a Seed Award in Science from the Wellcome Trust (204394/Z/16/Z).  
452 J.F.N. and E.G. are grateful to the Gut Human Organoid Platform (Gut-HOP) at King's College  
453 London, which is supported financially by a King's Together Strategic Award. M.D.A.N. is  
454 supported by a PhD studentship funded by the BBSRC London Interdisciplinary Doctoral  
455 Programme. E.R. acknowledges a Ph.D. fellowship from the Wellcome Trust (215027/Z/18/Z).  
456 S.L. gratefully acknowledges the UK Medical Research Council (MR/N013700/1) for funding  
457 through the MRC Doctoral Training Partnership in Biomedical Sciences at King's College  
458 London. G.M.L. is supported by grants awarded by the Wellcome Trust (091009) and the  
459 Medical Research Council (MR/M003493/1 & MR/K002996/1). N.J.W. acknowledges a Jane &  
460 Aatos Erkkö Foundation Personal Scholarship. R.M.P.dS acknowledges a King's Prize  
461 fellowship supported by the Wellcome Trust (Institutional Strategic Support Fund), King's  
462 College London and the London Law Trust. Via C.D.L.'s membership in the UK's HEC Materials  
463 Chemistry Consortium, which is funded by EPSRC (EP/L000202, EP/R029431), this work used  
464 the ARCHER UK National Supercomputing Service (<http://www.archer.ac.uk>) and the UK  
465 Materials and Molecular Modelling Hub (MMM Hub) for computational resources, which is  
466 partially funded by EPSRC (EP/P020194/1), to carry out the MD simulations. The authors also  
467 wish to thank the BRC flow cytometry core team, and acknowledge financial support from the  
468 Department of Health via the NIHR comprehensive Biomedical Research Centre award to Guy's  
469 and St. Thomas' NHS Foundation Trust in partnership with King's College London and King's  
470 College Hospital NHS Foundation Trust. The views expressed are those of the author and not  
471 necessarily those of the NHS, the NIHR, or the Department of Health. The authors thank  
472 Camilla Dondi, Daniel Foyt, and Oksana Birch for technical assistance. The authors are grateful  
473 to Dr. Jo Spencer and Dr. Kelly Schultz for helpful conversations about CD44 and  
474 microrheology, for technical support from Drs. Rebecca Beavil and Andrew Beavil with SEC-  
475 HPLC, Dr Hugo Sinclair from the Microscopy Innovation Centre for assistance acquiring  
476 microrheology data, Dr Richard Thorogate and the London Centre for Nanotechnology for  
477 assistance with AFM, Dr R. A. Atkinson and the NMR Facility of the Centre for Biomolecular  
478 Spectroscopy at King's College London, which was established with awards from the Wellcome  
479 Trust, British Heart Foundation and King's College London for assistance with NMR, and Simon

480 Engledow at the Oxford Wellcome Genomics Centre for processing the RNAseq samples.  
481 Finally, we would like to thank Dr. Luke Roberts, Erin Slatery, and Dr. Rocio Sancho for critically  
482 reading this manuscript and providing helpful feedback.

483

#### 484 Author contributions

485 G.M.J., M.D.A.N., T.T.L.Y., L.B., J.F.N. and E.G. developed experimental protocols, conducted  
486 experiments, and analyzed data. G.M.J. designed, conducted, and analyzed all murine and  
487 human experiments in Matrigel. T.T.Y.L., J.H., O.P.O., N.J.W., C.A.D., N.D.E., RMP.dS.  
488 designed and optimized the hydrogel synthesis. R.M.P.dS. designed peptide sequences.  
489 M.D.A.N., D.H., S.L., T.T.L.Y., G.M.J. and D.M., characterized the hydrogel. S.L. and C.D.L.  
490 performed the molecular dynamics simulations. G.M.J. and J.F.N. designed the RNA-  
491 sequencing experiment, and U.N. and M.C. provided bioinformatic analysis. G.M.J., P.R., E.R.,  
492 and T.Z. performed tissue isolations. G.M.J., M.D.A.N., and E.H. designed and conducted  
493 microrheology and AFM experiments. G.M.L., O.O., and D.D. contributed reagents, biopsies,  
494 and hiPSC lines. G.M.J., E.G. and J.F.N. conceived the ideas, initiated the project, interpreted  
495 the data, and prepared the manuscript. E.G. and J.F.N. supervised the project. All authors  
496 revised the manuscript.

497

#### 498 Data availability

499 The differentially expressed genes identified in the RNAsequencing dataset are available in  
500 Supplementary Data Set 1. The data have also been deposited with GEO at  
501 <https://www.ncbi.nlm.nih.gov/sra/?term=PRJNA641809> and  
502 [https://github.com/uhkniazi/BRC\\_Organoids\\_Geraldine](https://github.com/uhkniazi/BRC_Organoids_Geraldine). All other data supporting the findings of  
503 this study are available within the article and its supplementary information files or from the  
504 corresponding author upon reasonable request.

505

#### 506 Code availability

507 All code used to analyze the molecular dynamics simulations were tools that were built in-  
508 house. All codes with accompanying documentation as to how to use them is freely accessible  
509 at <https://github.com/Lorenz-Lab-KCL> and <https://nms.kcl.ac.uk/lorenz.lab/wp/>. R code for  
510 determining alpha from MSD data for microrheology is available in Supplementary Data Set 2  
511 and is freely accessible at <https://github.com/eileengentleman/Microrheology-code>.

512

#### 513 Competing interests



514 The authors declare no competing interests.

515

## 516 **Methods**

517

### 518 Establishment of murine SIO cultures

519 Organoid cultures were established by isolating intact small intestine crypts from 6-8 week  
520 female CD45.1 C57BL/6 mice following established protocols<sup>39</sup> and propagated in Matrigel  
521 (Corning) in basal media (DMEM/F12; 2mM Glutamax; 10mM HEPES; 1x Antibiotic-  
522 Antimycotic; 1x N2 supplement; 1x B27 supplement; all ThermoFisher, and 1mM Acetyl-L-  
523 cysteine, Sigma) supplemented with EGF (50ng/ml, R&D) and 50µl/ml of supernatant from both  
524 R-spondin (RSpo1-Fc) and Noggin cell lines, passaged every 4-5 days. RSpo1-Fc cell line was  
525 a kind gift from Professor Calvin Kuo and the Noggin cell line was a kind gift of Hubrecht  
526 Institute.

527

### 528 Murine intestinal lymphocyte isolation

529 Lamina propria ILC1 were isolated from small intestines of litter matched female RORγt-GFP  
530 reporter mice following established protocols<sup>40</sup>. In short, excess fat and Peyer's Patches were  
531 removed from the intestine, which was then opened longitudinally and rinsed thoroughly in ice-  
532 cold PBS. Small (1cm) sections were incubated in epithelial cell removal buffer for 2x15min  
533 (5mM EDTA and 10 mM HEPES in HBSS (GIBCO)), then tissue was cut into small pieces for  
534 extensive digestion of the extracellular matrix (collagenase (500µg/mL), dispase (0.5U/mL),  
535 DNase1 (500µg/ml), 2%FBS in HBSS (GIBCO)). Samples were filtered through a 40µm strainer  
536 in 10%FCS-DMEM10, then lymphocytes were isolated using a 80%/40% isotonic percoll density  
537 gradient separation (centrifuged at 900G for 25min, no acceleration or deceleration). The  
538 interphase between 40% and 80% percoll was collected, filtered, and prepared for FACS  
539 isolation of ILC1 without further enrichment. Next, lymphocytes were rinsed with PBS, then  
540 stained with fixable LIVE/DEAD UV (ThermoFisher) in PBS for 15min in the dark at 4°C. The  
541 dye was quenched with sorting buffer, then the Fc-receptor was blocked (CD16/CD32, clone 93)  
542 for 10min at 4°C, followed by extracellular staining following standard flow cytometry protocols  
543 (1µl antibody/100µl sorting buffer/5million cells unless otherwise indicated). FACS antibodies  
544 were sourced from eBioscience (with the exception of CD45) and were as follows: CD3-  
545 Fluor450 (RB6-8C5), CD5-Fluor450 (53-7.3), CD19-Fluor450 (eBio1D3), Ly6G-Fluor450 (RB6-  
546 8C5), CD45-BV510 (30-F11, bioLegend) CD127-APC (A7R34), KLRG1-PerCP/eFluor710  
547 (2F1), NKp46-PE/Cyanine7 (29A1.4), NK1.1-PE (PK136). Cells were rinsed, and sorted on a

548 70µm nozzle after calculation of compensation, and acquisition of Fluorescence Minus One  
549 controls for Lineage, CD127, and NKp46. Gating strategies are outlined in Supplementary  
550 figures.

551

#### 552 Murine ILC-organoid co-cultures

553 Approximately 1500-2500 murine ILC1 were seeded with ~100 mechanically disrupted SIO  
554 crypts per well, resuspended in 30µl ice-cold Matrigel, pipetted onto pre-heated tissue culture  
555 plates (Nunclon) and incubated at 37°C for 15-20min prior to addition of pre-warmed basal  
556 media supplemented with 50mM B2ME (R&D), 20ng/ml rhIL-2 (Sigma), 20ng/ml rmIL-7 (R&D),  
557 and 1ng/ml IL-15 (R&D), with media changes every 2-4 days.

558

#### 559 Human iPSC-derived intestinal organoids

560 The healthy KUTE-4 female skin fibroblast-derived human iPSC (hiPSC) line (available from the  
561 European Collection of Authenticated Cell Cultures (karyotyped, passage 24-36)) was cultured  
562 on plates coated with 40µl/ml vitronectin in PBS (StemCell Technologies). E8 (Gibco) media  
563 was changed daily, pockets of differentiation were actively removed, and round, pluripotent  
564 colonies were passaged with Versene (Gibco) every 4-6 days, when 60-70% confluent, or  
565 before circular colonies began merging.

566 KUTE-4 hiPSC were differentiated into human small intestine organoids (HIO) following  
567 established protocols<sup>18</sup>. In short, hiPSC were patterned toward definitive endoderm in RPMI with  
568 daily increasing B27 (0.2%, 1%, 2%) and 100ng/ml ActivinA (R&D) for 3.5 days, then patterned  
569 towards midgut in RPMI+2%B27 with 3µM CHIR99021 (Wnt agonist, TOCRIS) and 500ng/ml  
570 recombinant FGF4 (R&D) for 4days. At this point, CDX2 colonies were picked using a 200µl  
571 pipette tip, replated in 35µl Matrigel, then matured in basal media with hEGF 100ng/ml, R&D)  
572 rh-Rspondin (500ng/ml, R&D), rh-Noggin (100ng/ml, R&D), and 2ng/ml IL-2 supernatant for at  
573 least 35 days prior to establishing co-cultures with hILC1 or encapsulation in synthetic hydrogels  
574 for aILC1 characterization.

575

#### 576 Human lymphocytes isolation from patient biopsies

577 Studies in human tissues received ethical approval from the London Dulwich Research Ethics  
578 Committee (REC reference 15/LO/1998). Informed written consent was obtained in all cases.  
579 Inflammatory status of IBD patients was diagnosed by a consultant, and 15-20 colonic biopsies  
580 were procured by endoscopy. These were cultured on rat tail collagen I coated 9mm x 9mm x  
581 1.5mm Cellfoam matrices (Cytomatrix PTY Ltd) in complete media (RPMI with 10% FBS) with

582 antibiotics (penicillin, streptomycin, metronidazole, gentamicin and amphotericin) for 48h  
583 following established protocols<sup>41, 42</sup>. Colonic lamina propria mononuclear cells (cLPMCs) were  
584 then isolated from the supernatant ready for evaluation<sup>43</sup> (protocol adapted from Di Marco  
585 Barros *et al*). Then, cLPMC were rinsed with PBS, treated with fixable Live/Dead-UV, and Fc  
586 blocked before being stained with CD45-eFluor450 (HI30; Invitrogen), Lineage cocktail 3-FITC  
587 (CD3, CD14, CD19, CD20; BD Biosciences), CD4-FITC (OKT4; BioLegend), TCR $\alpha/\beta$ -FITC  
588 (IP26; Biolegend), TCR $\gamma/\delta$ -FITC (B1; Biolegend), CD56-Alexa700 (B159; BD Pharmingen),  
589 CD7-PE-CF594 (M-T701; BD Horizon), CD127-PE-Cy7 (eBioRDR5; Invitrogen), c-kit-BV605  
590 (104D2; BioLegend), CRTH2-PE (MACS Milltenyi Biotec), and CD161-APC (HP-3G10;  
591 BioLegend). cLPMC were sorted on a 70 $\mu$ M nozzle on Aria2 (BD) using BD FACS Diva 8.0.1  
592 software. One biopsy per patient was fixed in 4%PFA and maintained for histology.

593

#### 594 Human ILC1-organoid co-cultures

595 Approximately 15-30 mature HIO were added to eppendorfs containing 50-300 hILC1 directly  
596 after FACS isolation from biopsies. The two components were centrifuged at 500G for 3min,  
597 supernatant was carefully removed, and the co-cultures were resuspended in 35 $\mu$ l Matrigel and  
598 plated onto pre-warmed tissue culture treated plates. The same culture conditions optimized for  
599 murine co-cultures were used for HIO-hILC1 co-cultures, including 50mM B2ME (R&D), 20ng/ml  
600 rhIL-2 (Sigma), 20ng/ml rmlL-7 (R&D), and 1ng/ml IL-15 (R&D), with media changes every 3-4  
601 days.

602

#### 603 Cell isolation from co-cultures

604 After 4 days of murine and 7 days of human co-culture, Matrigel was disrupted and cells were  
605 collected into 15ml falcon tubes. For murine ILC1 cultures Matrigel disruption was not required,  
606 and cells were gently rinsed from the bottom of the plate using PBS+2%FCS. Samples were  
607 rinsed with PBS, then dissociated in TrypLe (Gibco) for 20mins at 37°C. The sorting buffer after  
608 this step contained DNase (250 $\mu$ g/ml), EDTA (1 $\mu$ l/ml), and HEPES (1 $\mu$ l/ml) to maintain single  
609 epithelial cells and avoid clumping. Cells were titrated gently, centrifuged and resuspended in  
610 sorting buffer. Cells were then filtered (70 $\mu$ m), having pre-coated the filter with sorting buffer to  
611 minimize cell loss, and either rinsed with PBS for fixable Live/Dead staining (UV or  
612 nearInfraRed, Thermofisher), or stained with EpCAM, CD45, and the requisite combination of  
613 antibodies for the experiment, and analyzed (BD Fortessa) or sorted (BD ARIA3 Fusion & BD  
614 Aria 2 using BD FACS Diva 8.0.1 software). Isolation of murine IEC and ILC1 following co-  
615 culture was performed using EpCAM-APC Cy7 (G8.8, BioLegend), CD45-BV510 (30-F11,

616 bioLegend), NK1.1 BV605 (PK136, BioLegend), CD44-PE (IM7, BioLegend). Isolation of human  
 617 IEC, FB, and hILC1 used fixable Live/Dead-UV or Live/Dead-nIR CD45-eFluor450(HI30)  
 618 Invitrogen, EpCAM-FITC (9C4; BioLegend), CD90-PE/Dazzle (Thy1; BioLegend)

619

620 Flow cytometry

621 Flow cytometry data were acquired on a BD Fortessa2 and analyzed using FlowJo v10.5.3.

622

623 RT-qPCR

624 For RNA isolation, cells were FACS-sorted directly into 250µl RLT (Qiagen) lysis buffer  
 625 supplemented with 10µl/ml BME to stabilize the RNase-rich intestinal epithelial tissue lysate.  
 626 RNA was isolated using the RNeasy MicroRNA isolation kit (QIAGEN), and cDNA produced  
 627 using RevertAid (Fisher), using oligo dTTTTT primers. Fast SYBR-green mix (Applied  
 628 Biosystems) based RT-qPCR were run on a CFX384 Touch™ Real-Time PCR Detection  
 629 System (BioRad), with no-template controls (NTC) and melting curves for quality control, or  
 630 using TaqMan Gene Expression Master Mix (Applied Biosystems) with FAM-probes, using an  
 631 annealing temperature at 60°C for 39 cycles. All kits were used following manufacturers'  
 632 instructions. Primers were designed using PrimerBank and verified via BLAST against the *Mus*  
 633 *musculus* or *Homo sapiens* genome on ensemble.org. Cq values were normalized to the  
 634 housekeeping genes *Hprt1* or *GAPDH* for SYBR and *HPRT1* for TAQ probes.

635

Target	Forward (5'-3')	Reverse (5'- 3')
<i>Tgfb1</i>	CTTCAATACGTCAGACATTCGGG	GTAACGCCAGGAATTGTTGCTA
<i>Cd44s</i>	TCGATTTGAATGTAACCTGCCG	CAGTCCGGGAGATACTGTAGC
<i>Cd44v4</i>	CCTTGGCCACCATTGCAAG	CAGCCATCCTGGTGGTTGTC
<i>Cd44v6</i>	CCTTGGCCACCACTCCTAATAG	CAGTTGTCCCTTCTGTCACAT
<i>Mmp9</i>	CACCAAAGTGGATGACGATG	CACCAAAGTGGATGACGATG
<i>Hprt1</i>	TGGATACAGGCCAGACTTTGTT	CAGATTCAACTTGCGCTCATC

636

**Human SYBR**

<b>Target</b>	<b>Forward (5'-3')</b>	<b>Reverse (5'-3')</b>
<i>TGFB1</i>	CTAATGGTGGAAACCCACAACG	TATCGCCAAGGAATTGTTGCTG
<i>FN1</i>	CGGTGGCTGTCAGTCAAG	AAACCTCCGGCTTCCTCCATAA
<i>CD44s</i>	AGTGAAAGGAGCAGCACTTCA	GGTCTCTGGTAGCAGGGATTC
<i>CD44v4</i>	AGTGAAAGGAGCAGCACTTCA	GGTTGAAATGGTAGCAGGGATTC
<i>CD44v6</i>	AGTGAAAGGAGCAGCACTTCA	GCCTGGATGGTAGCAGGGATTC
<i>MMP9</i>	GGGACGCAGACATCGTCATC	TCGTCATCGTCGAAATGGGC
<i>CDX2</i>	GACGTGAGCATGTACCCTAGC	GCGTAGCCATTCCAGTCCT
<i>SOX17</i>	GTGGACCGCACGGAATTTG	GGAGATTCACACCGGAGTCA
<i>FOXA2</i>	GGAGCAGCTACTATGCAGAGC	CGTGTTTCATGCCGTTTCATCC
<i>GATA4</i>	CGACACCCCAATCTCGATATG	GTTGCACAGATAGTGACCCGT
<i>VILLIN</i>	ACCTTGTGCTCTACACATACCA	CATGACATCTAGTTCCTCAGCG
<i>APOA4</i>	AACTCACCCAGCAACTCAATGCC	CTCCTTCCCAATCTCCTCCTTCAG
<i>LYZ1</i>	TCAATAGCCGCTACTGGTGTA	ATCACGGACAACCCTCTTTGC
<i>OCT4</i>	GACAGGGGGAGGGGAGGAGCTAGG	CTTCCCTCCAACCAGTTGCCCAA AC
<i>GAPDH</i>	TGTGTCCGTCGTGGATCTGA	TTGCTGTTGAAGTCGCAGGAG

637

### Human TAQ

<i>IFNG</i>	Hs00989291_m1 20x	Lot:P190527
<i>IL22</i>	Hs01574154_m1 20x	Lot:1661859
<i>TGFB1</i>	Hs00998133_m1 20x	Lot:1587597

<i>HPRT1</i>	Hs99999909_m1 20x	Lot:1610327
--------------	-------------------	-------------

638

639

640 Cytokine quantification

641 TGFβ-1 concentration in supernatant from 4day ILC1 co-cultures and SIO-only controls was  
642 measured using the Mouse TGFβ-1 DuoSet ELISA (R&D Systems) with modified  
643 manufacturer's instructions, whereby 100μl supernatant was incubated with the capture  
644 antibody overnight on a shaker at 4°C, not for 2h at RT. Optical density was measured in a plate  
645 reader (BioRAD) at 450nm, with correction at 540nm. Concentrations were obtained based on a  
646 regression equation (multimember regression, order 3) from the standard curve values  
647 (calculated in Microsoft Excel, version 16.16.20).

648

649 Cytometric Bead Array for Th1/Th2/Th17 cytokines was obtained from BD biosciences and  
650 performed on 10μl supernatant after 4day co-culture following the manufacturers' instructions,  
651 using a BD Fortessa2, and analyzed following the manufacturers' template based on a standard  
652 curve for each cytokine.

653

654 PEG-peptide conjugate synthesis/characterization and hydrogel formation

655 Custom-designed peptides (supplied as either trifluoroacetic acid or acetate salts) used to either  
656 create A<sub>2</sub>+B<sub>4</sub> (Ac-CREW-ERC-NH<sub>2</sub>) or A<sub>4</sub>+B<sub>4</sub> designs containing either a degradable (Ac-  
657 GRDSGK-GPQG↓IWGQ-ERC-NH<sub>2</sub>), non-adhesive/non-degradable (non-adh/non-deg, Ac-  
658 KDW-ERC-NH<sub>2</sub>) or adhesive sequence (RGD, presented in either a linear Ac-RGDSGK-  
659 GDQGIAGF-ERC-NH<sub>2</sub> or loop configuration (RGDSGD)K-GDQGIAGF-ERC-NH<sub>2</sub>) were  
660 synthesized by Peptide Protein Research, Ltd (UK) (all >98% purity). To create PEG-peptide  
661 conjugates, peptide was dissolved in anhydrous dimethyl sulfoxide (DMSO) at 10mg/ml and  
662 anhydrous triethylamine (TEA) (both Sigma) was added stoichiometrically to convert the peptide  
663 salts into their free forms in order to deprotonate the primary amine from the lysine side chain.  
664 Peptides were then conjugated to star-shaped, 4-arm PEG activated at each terminus with  
665 nitrophenyl carbonate (PEG-4NPC) by a nucleophilic substitution reaction between the primary  
666 amine on the side chain of the lysine residue of each peptide and NPC esters, forming stable  
667 carbamate linkages. To accomplish this, a 16.67mg/ml solution of 10K PEG-4NPC (JenKem  
668 Technology, USA) in DMSO was reacted with peptide on an orbital shaker at either a 12:1 ratio  
669 of excess peptide to PEG-4NPC at RT for 30min (non-adh/non-deg), a 10:1 ratio at 60°C for 3h

670 (degradable), a 8:1 ratio at RT for 2h (cyclic adhesive), or a 4:1 ratio at RT for 30min (linear  
671 adhesive). Conjugates were then snap frozen on dry ice and lyophilized. To reduce disulfide  
672 bonds, conjugates were dissolved in carbonate-bicarbonate buffer at pH9.0 and treated with  
673 DTT (0.1g/ml) for 6h at RT, after nitrogen purging (molar ratio of 4.5:1, DTT:peptide).  
674 Conjugates were then purified 4x in MiliQ water using Merck Millipore Ultrafiltration 1MWCO  
675 units (10KDa cut-off), snap frozen and lyophilized again prior to storage at -20°C

676

677 Conjugation conversion was determined for non-adh/non-deg, degradable and cyclic adhesive  
678 conjugates by size exclusion chromatography (SEC) using a Gilson HPLC system. Calibration  
679 was performed using standards of known peptide concentration. The relative amount of  
680 unreacted peptide was assessed by estimating the concentration of free peptide in the crude  
681 reaction mixture. We observed that 77-87% of PEG arms were conjugated with peptide and that  
682 the conjugation efficiency was 81-91%.

683

684 Hydrogels with an A<sub>4</sub>+B<sub>4</sub> design were formed by reacting PEG-peptide conjugates with star-  
685 shaped 4-arm PEG (20kDa, unless otherwise noted) bearing vinyl sulfone groups at each chain  
686 terminus (PEG-4VS). The reaction was performed in a stoichiometric ratio of 1:1 in 30 mM  
687 HEPES buffer (pH8.0, with 1X HBSS in a desired volume) through a Michael-type reaction  
688 between a cysteine thiol on the C-terminal of the peptide with the vinyl-sulfone group on PEG-  
689 4VS. To form 2.5% non-adh/non-deg hydrogels for swelling and rheological studies using an  
690 A<sub>2</sub>+B<sub>4</sub> design, Ac-CREW-ERC-NH<sub>2</sub> was reacted with PEG-4VS in a stoichiometric ratio of 2:1 in  
691 30mM HEPES buffer (pH8.0). Hydrogels were then allowed to form for 45-60min prior to being  
692 placed in PBS/culture media as indicated.

693

694 The conjugation efficiency of the thiol vinyl sulfone reaction was determined using proton NMR  
695 and Ellman's assay. For <sup>1</sup>H NMR experiments, PEG-peptide conjugate and PEG-4VS were  
696 dissolved separately in HEPES buffer and lyophilized. The resulting powders were dissolved  
697 separately in deuterium oxide to a final polymer/peptide concentration of 1.5 wt%, mixed at  
698 stoichiometric ratio and loaded into 0.3mm diameter NMR tubes. Acquisition of spectra was  
699 performed on a Bruker 700MHz NMR spectrometer. The first measurement was made after 6  
700 min and additional measurements collected for up to 1h when aromatic signals from the vinyl  
701 sulfone were no longer distinguishable. Hydrogel formation was observed inside the NMR tubes  
702 at the end of the experiment.

703

704 The relative quantity of free thiols during the reaction were quantified using the molar  
705 absorptivity of Ellman's reagent, as previously described. Briefly, a 4 mg/ml solution of Ellman's  
706 reagent was prepared in reaction buffer (0.1M PBS, pH8.0, containing 1mM EDTA). Hydrogels  
707 were prepared and the cross-linking reaction halted after 5, 10, 15, 30 and 60min using a 1:50  
708 dilution of reaction buffer and Ellman's reagent solution. Samples were then incubated for 15min  
709 and absorbance measured at 412nm. Free thiols in a peptide (Ac-KDWERC-NH2) solution  
710 alone were quantified using the same method. The concentration of free thiols was calculated  
711 based on the molar extinction coefficient of Ellman's reagent ( $14150 \text{ M}^{-1} \text{ cm}^{-1}$ ) and Equation 1:

$$712 \quad c=A/b\epsilon$$

713 Where A is the absorbance of the sample at 412nm, b is 1cm and  $\epsilon$  is the molar extinction  
714 coefficient.

715

### 716 Molecular dynamics simulations

717 Coarse-grain classical molecular dynamics simulations were used to study the cross-linking of  
718 hydrogels formed with either  $A_4+B_4$  or  $A_2+B_4$  designs. Three hydrogel systems were simulated  
719 in replicate: Ac-KDWERC-NH2 and H-SREWERC-NH2 are  $A_4+B_4$  designs and Ac-CREWERC-  
720 NH2 is an  $A_2+B_4$  design. As in our experimental work, Ac-KDWERC-NH2 and H-SREWERC-  
721 NH2 are 'pre-conjugated' in the simulation to PEG-4NPC and the reaction with PEG-4VS is  
722 simulated. For Ac-CREWERC-NH2, there was no 'pre-conjugation' step and PEG-4VS was  
723 allowed to react with the free peptide. Ac-KDWERC-NH2 is the non-adh/non-deg peptide used  
724 in experimental studies; however, as the net charge of Ac-KDWERC-NH2 is -1, while that of Ac-  
725 CREWERC-NH2 is 0, we also simulated the  $A_4+B_4$  system with H-SREWERC-NH2 (net charge  
726 of 0) to study our system independently of electrostatic bias in bond formation. Supplementary  
727 Figure 17 summarizes the molecules and water beads used in each simulated system. As we  
728 have used the MARTINI forcefield to represent the peptide cross-linkers, ions and the water  
729 molecules, each water bead represents 4 water molecules. The PEG molecules were modelled  
730 with the MARTINI-like forcefield, as described in Lee et al. (2009)<sup>41, 44</sup>.

731

732 The initial systems were built using PACKMOL (version 18.104)<sup>42</sup> to randomly place each  
733 component within a 40nm x 40nm x 40nm simulation box. The LAMMPS simulation engine was  
734 used for all simulations<sup>45</sup>. The software package Moltemplate (version 2.7.3) was used to<sup>45</sup>  
735 convert the configurations generated by PACKMOL to those readable by LAMMPS. The  
736 resulting systems have PEG concentrations of 2.5%. Once the initial systems were built, we first  
737 minimized energy using the steepest descent algorithm with an energy tolerance of  $1 \times 10^{-4}$  and



738 a force tolerance of  $1 \times 10^{-6}$ . The systems were then equilibrated by carrying out a series of  
739 simulations with the NVT (constant number of particles, volume and temperature) ensemble  
740 with the Langevin thermostat and a target temperature of 300K. During these simulations, the  
741 systems were run for 1ps with a 1fs timestep, 3ps with a 3fs timestep, 10ps with a 10fs timestep  
742 and then 400ps with a 20fs timestep. The volume was then equilibrated by carrying out a series  
743 of simulations with the NPT (constant number of particles, pressure and temperature) ensemble  
744 employing the Langevin thermostat and the Parrinello-Rahman barostat. In these simulations,  
745 the time step was again increased (1ps with a 1fs timestep, 3ps with a 3fs timestep, 10ps with a  
746 10fs timestep, and 2ns with a 20fs timestep). The densities of the systems were then  
747 equilibrated using the NPT ensemble with a Nosé-Hoover thermostat and barostat for a  
748 simulation lasting 2ns with a 20fs timestep. Finally, we equilibrated the temperature of the  
749 simulated systems to 450K using an NVT simulation with the Nosé-Hoover thermostat which  
750 lasted 40ns with a 20fs timestep.

751  
752 Production simulations were carried out in the NVT ensemble at 450K (to increase diffusion and  
753 allow for investigation of hydrogel cross-linking in a reasonable amount of simulation time) with  
754 a timestep of 20fs. During simulations, we employed cross-linking methods that have been  
755 previously shown in simulations to lead to the formation of hydrogels<sup>46</sup>. In short, we identify  
756 beads that can react with one another and then check at regular time intervals ( $t_{\text{react}}$ ) if any two  
757 reaction partner beads are within a given distance ( $r_{\text{react}}$ ) of one another. If so, then a new bond  
758 is formed with a given probability ( $p_{\text{react}}$ ). Here, we used a bead containing the sulphur atom  
759 within the cysteine residue on each peptide as a reactive bead in the simulations. Its reaction  
760 partner was the terminal bead on each arm of PEG-4VS. This reaction model is consistent with  
761 the chemistry that forms the hydrogels. The reactions were modelled using  $t_{\text{react}} = 20\text{ps}$ ,  $r_{\text{react}} =$   
762  $5.0\text{\AA}$  and  $p_{\text{react}} = 0.5$ . Once a bond was formed between any cysteine bead and a terminal bead  
763 on a PEG-4VS, neither of those beads could form any other new bonds during the simulation.  
764 Production simulations were run for at least  $5.5\mu\text{s}$  seconds for 1 replica of each system, and the  
765 other replica was run for  $\sim 4\mu\text{s}$ .

766

767 Measurements of hydrogel swelling

768 30µl hydrogels were formed in Sigmacote®-treated 6mm diameter glass cylindrical moulds and  
769 submersed in PBS. Hydrogel weight was monitored, and the wet weight measured once  
770 swelling equilibrium had been achieved (after 48h). Hydrogels were then lyophilized to  
771 determine dry weight and the mass swelling ratio ( $Q_m$ )  
772 calculated using Equation 2:

$$Q_m = \text{Wet weight} / \text{Dry weight}$$

774  
775

#### 776 Rheological measurements of hydrogel gelation

777 Hydrogel gelation was assessed on a strain-controlled ARES from TA Instruments using a  
778 25mm cone with a 0.02rad cone-and-plate by carrying out small amplitude oscillatory time  
779 sweep measurements at a strain of 5% and a constant angular frequency of 1rad/s. All  
780 measurements were carried out at 37°C, sealing the chamber with oil to prevent evaporation. To  
781 perform measurements, 80µl hydrogels were placed in the instrument and storage modulus  $G'$   
782 and loss modulus  $G''$  were recorded as a function of time in Orchestrator (version 7.0) software.  
783 Subsequently an amplitude sweep was carried out, recording  $G'$  and  $G''$  as a function of shear  
784 amplitude in the range of 1-100% shear strain, to determine the linear viscoelastic region.  
785 Finally, a frequency sweep was recorded, measuring  $G'$  and  $G''$  as a function of shear frequency  
786 in a range of 100 - 0.1rad/s, to assess the hydrogels' temporal behaviour.

787

#### 788 Quantification of MMP-mediated hydrogel degradation

789 Degradability was assessed on 30µl hydrogels formed with either 0, 45, 75, or 100% of PEG-  
790 peptide conjugates containing a degradable sequence (all other cross-links formed with non-  
791 adh/non-deg peptides) that had been allowed to swell in PBS for 24h. To degrade hydrogels,  
792 PBS was replaced with a solution of TCNB buffer (50mM Tris, pH7.5, with 100mM NaCl, 10mM  
793  $\text{CaCl}_2$ ) containing 89.5 nM human MMP9 (Sigma SAE0078) and incubated at 37°C.  
794 Degradation was determined by measuring the absorbance of tryptophan found on the cleaved  
795 peptide section in the supernatant at 280nm. Degradation was determined by calculating the  
796 ratio of the cleaved peptide in solution to that in the initial hydrogel.

797

#### 798 Mechanical testing by atomic force microscopy (AFM)-based indentation

799 30µl hydrogels were formed in Sigmacote®-treated 6mm diameter glass cylindrical moulds in  
800 35mm petri dishes and stored in PBS at 4°C prior to testing. Force-distance measurements  
801 were carried out on a JPK Nanowizard 4 (JPK instruments AG, DE) directly on hydrogels

802 immersed in PBS at RT. To perform indentation measurements, spherical glass beads  
803 (diameter 10 $\mu$ m; Whitehouse Scientific, UK) were mounted onto tipless triangular silicon nitride  
804 cantilevers (spring constant (K)  $\approx$  0.12 N m<sup>-1</sup>; Bruker AXS SAS, FR) using UV-cross-linked  
805 Loctite super glue. The deflection sensitivity of the AFM photodiode was then calibrated by  
806 collecting a single force-distance curve on a glass slide. Cantilevers were calibrated using the  
807 thermal method<sup>47</sup> in air. Measurements were made on 6 different locations across each  
808 hydrogel's surface (100 $\mu$ m x 100 $\mu$ m areas, 100 force curves per location on 3 independent  
809 hydrogels per condition). Indentations were carried out with a relative setpoint force of 3nN and  
810 a loading rate of 4 $\mu$ m s<sup>-1</sup>. Data were collected using JPK proprietary SPM software (version 6.1,  
811 JPK Instruments AG, DE). The Oliver–Pharr model for a spherical tip was used to determine E.  
812 Outliers were removed using a ROUT test (Q=1%). As for other hydrated biological samples, we  
813 assumed that volume was conserved and assigned a Poisson's ratio of 0.5.

814

#### 815 Human ancillary ILC1 hydrogel co-cultures

816 HIO were harvested, titrated, and thoroughly rinsed with ice cold PBS, then resuspended in  
817 pH8.0 buffered phenol free and protein free HBSS (pH8-HBSS, Gibco), spun down,  
818 resuspended and left on ice until encapsulation. PEG-peptide conjugates were dissolved in ice  
819 cold pH8-HBSS, vortexed and centrifuged, and combined based on the gel composition (e.g.  
820 IM-DEG: 20% cyclic adhesive, 45% DEG, 35% NON-DEG). An equal molar mass of PEG-4VS  
821 was weighed in a protein-low-binding eppendorf, dissolved in pH8-HBSS, centrifuged and  
822 added to the PEG-conjugate mix, and the sample was vortexed and centrifuged again. HIO  
823 were then rapidly mixed into the PEG-peptide conjugate/PEG-4VS mix using protein-low binding  
824 200 $\mu$ l tips, and pipetted into a pre-warmed, Sigmacote®-treated glass ring in a 24-well plate  
825 Nunclon well. HIO-laden gels were incubated at 37°C and after 30min the glass ring was  
826 removed using an autoclaved forceps. Basal media supplemented with 50mM BME, 20ng/ml IL-  
827 2, 20ng/ml IL-7, and 1ng/ml IL-15 (R&D), containing FACS-isolated human ILC1 from inflamed  
828 biopsies was added to the cultures.

829

#### 830 Stiffness mapping of IM-DEG hydrogel-HIO cultures by AFM

831 Organoids were encapsulated in IM-DEG hydrogels formed in Sigmacote®-treated 10mm  
832 diameter glass cylindrical moulds and submersed in culture media. Force-distance curves were  
833 collected on a JPK Nanowizard-CellHesion (JPK instruments AG, DE) mounted onto an inverted  
834 light microscope. Tipless triangular silicon nitride cantilevers (spring constant (K)  $\approx$  0.12 N m<sup>-1</sup>;  
835 Bruker AXS SAS, FR) were calibrated using the thermal method<sup>47</sup> in air and then functionalized

836 with 50 $\mu$ m silica beads (Cospheric, USA) as above. Prior to measurements, the deflection  
837 sensitivity of the AFM photodiodes was calibrated by collecting a single force-distance curve on  
838 a glass slide in liquid.

839

840 Prior to measurements, cultures containing organoids were placed in CO<sub>2</sub> independent media  
841 (Sigma). Maps were then collected across the surface of hydrogels in regions where an  
842 organoid could be clearly identified on the inverted light microscope. Map sizes varied  
843 depending on the organoid size but indentations were done in either 8x8 or 16x16 grids with the  
844 largest map being 300x300 $\mu$ m and the smallest 150x150 $\mu$ m. For each map, indentations were  
845 carried out at a relative setpoint of 2.5nN and a loading rate of 4 $\mu$ m s<sup>-1</sup>. The manufacturer's  
846 proprietary JPK SPM software (version 6.1, JPK Instruments AG, DE) was used to determine *E*  
847 using the Hertz model for a spherical tip. As for other hydrated biological samples, we assumed  
848 that volume was conserved and assigned a Poisson's ratio of 0.5.

849

#### 850 Multiple particle tracking microrheology

851 0.75 $\mu$ m diameter fluorescent beads (Fluoresbrite YG Carboxylate Kit I 21636-1, Polysciences  
852 Inc.) were suspended at a concentration of 0.04% (w/w) in the polymer solution within 5-10 $\mu$ l  
853 HIO-laden hydrogels with or without aILC1. Samples were prepared and imaged in Ibidi slide-  
854 chambers ( $\mu$ -Slide Angiogenesis, 81501) using a modified setup and analysis pipeline to that  
855 previously described by Schultz et al.<sup>28</sup>. Approximately 7-10 HIO were embedded in each  
856 hydrogel.

857

858 Time-lapses of moving beads were acquired using an Olympus TIRF System using an  
859 excitation of 488nm. Time-lapses of 800 frames were collected at a rate of 16.9ms per frame  
860 and exposure time of 1.015ms. HIO images were also captured in brightfield. 3-8 experimental  
861 measurements were made for each sample. TrackMate (Fiji, version 4.0.1) was used to  
862 segment beads and create trajectories across the 800 frames. Mean squared displacements of  
863 individual beads were then calculated from the TrackMate output using custom R-script  
864 (Supplementary Data Set 2).

865

#### 866 Immunocytochemistry

867 Co-cultures were fixed for 10min using 4%PFA and either stained as whole organoids in FCS-  
868 coated Eppendorf tubes, or cryoprotected (overnight 30% glucose for organoids in Matrigel,  
869 overnight OCT replacement for hydrogels) and embedded in OCT for cryosectioning on a

870 Penguin cryostat. Images were acquired on an inverted Leica SP8 inverted confocal  
871 microscope. Cells were blocked with 2%FCS and 0.05%TRITON-X in PBS for 1h at RT, stained  
872 at 4°C overnight, and in secondaries (ThermoFisher) for 1h at RT, followed by extensive rinse  
873 steps. Heat Antigen Retrieval was performed in pH8.0 basic conditions (10min, 95°C waterbath)  
874 for CD44v6 staining to reveal the v6 epitope, and optimize signal strength. All secondary  
875 antibodies were AlexaFluor conjugate dyes (488, 555, or 647) raised in donkey (ThermoFisher)  
876  
877 Image processing and quantification was performed using Fiji (version 1.0, ImageJ). Image  
878 quantification was performed on max-intensity projections with the same (i) number of Z- stacks  
879 and (ii) the same brightness and contrast settings in each fluorophore channel, having been  
880 taken with the same laser power and gain values. Background intensity of the channel was  
881 subtracted from average intensity, which was then normalized to DAPI (nuclear) intensity.  
882 Nuclear phosphorylated p38 (p-p38) was quantified as follows: DAPI channel was processed to  
883 “binary” and erosion (E) and dilation (D) operations were performed to homogenize the nucleus  
884 area (E, D, D, E). An overlay with the outlines of the nuclei was created and saved in the ROI  
885 manager, which was then superimposed to either p-p38 channel. The mean intensity of each  
886 fluorophore within the defined nuclei areas was measured, giving an approximate measure of  
887 intensity values/nuclei.

888  
889 Antibodies used were as follows:  
890

Target	Host species	Provider	Cat#	Reactivity	Dilution
Fibronectin	Rabbit	abcam	Ab2413	Human, Mouse	1:1000
CD45 (HI30)	Mouse	BioLegend	304001	Human	1:500
FoxA2	Rabbit	Abcam	Ab108422	Human	1:100
CDX2	Rabbit	Abcam	Ab76541	Human	1:250
Lysozyme	Rabbit	Invitrogen	PA5-16668	Human, Mouse	1:500
E-Cadherin (DECMA-6273)	Rat, (Alexa647)	eBioscience	51-3249-82	Human	1:250

1)					
$\beta$ -catenin	Mouse	BD Biosciences	610153	Human, Mouse	1:100
CD44 (IM7)	Rat	eBioscience	14-0551-82	Human, Mouse	1:250
EpCAM	Rabbit	abcam	Ab71916	Human, Mouse	1:750
GATA4	Mouse	Santa Cruz	Sc-25310	Human	1:500
SOX17	Goat	R&D	Af1924	Human	1:500
Vimentin	Chicken	Millipore	Ab5733	Human, Mouse	1:1000
TGF $\beta$ R1	Rabbit	Santa Cruz	Sc-339	Human, Mouse	1:500
ZO-1	Rabbit	ThermoFisher	61-7300	Human, Mouse	1:100
Phos- p38 (Thr180/Tyr182)	Rabbit	Cell Signalling	4511	Human, Mouse	1:250
Phalloidin-TexRed (F-Actin)	N/A	ThermoFisher	T7471	Human, Mouse	1:5000
DAPI	N/A	ThermoFisher	D1306	Human, Mouse	1:5000
CD44var6 (VFF-18)	mouse	ThermoFisher	BMS125	Human	1:500
CD44v6 (9A4)	Rat IgG1	BioRad	MCA1967	Mouse	1:500
SMA	Mouse IgG <sub>2A</sub>	R&D	MAB142	Human/Mouse/Rat	1:1000
$\beta$ -catenin	goat	R&D	AF1329	Human/Mouse/Rat	1:500

891

892

893 Viability tests

894 Single cell viability distinguishing between epithelial cells (EpCAM<sup>+</sup>, CD90<sup>-</sup>) and Fibroblasts  
895 (EpCAM<sup>-</sup>, CD90<sup>+</sup>) was performed using the fixable Live/Dead near InfraRead viability kit  
896 (ThermoFisher). Encapsulated HIO were rinsed with PBS, then treated with 0.025% Trypsin-  
897 EDTA (Gibco) for 10-20min at 37°C to dissociate both the hydrogel and the HIO. HIO were then

898 rinsed with PBS, stained with Live/Dead nIR for 15min at 4°C in the dark, then stained for 20min  
899 with EpCAM-FITC and CD90-PE-Dazzle for 20min at 4°C in the dark in PBS with 2% FCS.  
900 Dissociated HIO were analyzed on a BD Fortessa 2. Whole HIO viability within the gel was  
901 assessed by rinsing the gel twice with PBS, then staining HIO with 5mg/ml Fluorescein Diacetat  
902 (FDA; Sigma-Aldrich Co. LLC, C-7521) and 2mg/ml Propidium Iodide (Sigma-Aldrich Co. LLC,  
903 P4170) in PBS for 2min while gently shaking, followed by two rinse steps with PBS. HIO-  
904 hydrogel conditions were treated and imaged one and at a time, and images acquired within 1-  
905 10min of FDA/PI treatment to ensure comparable FDA levels were acquired and no excess  
906 cytotoxicity was induced through the treatment process. Images were captured at 20X on a  
907 Leica SP8 confocal microscope, and only HIO at the bottom of the gel within complete z-stack  
908 range were acquired. Flow cytometry was quantified with FlowJo (version 10.5.3), images were  
909 quantified using Fiji (version 1.0).

910

#### 911 Production of RNAseq dataset

912 The cells were harvested as described above for sorting by flow cytometry (BD ARIA3 Fusion  
913 using BD FACS Diva 8.0.1 software) into RLT (Qiagen) lysis buffer. RNA was harvested using  
914 RNeasy MicroRNA isolation kit (QIAGEN), and RIN values were assessed using RNA 6000  
915 Pico Kit (Agilent). The library was prepared using SMARTSeq2 and sequenced by Illumina  
916 HiSeq 4000 at the Wellcome Trust Oxford Genomics Core, where basic alignment  
917 (GRCm38.ERCC (2011)) and QC was also performed.

918

#### 919 RNAsequencing data analysis

920 Exploratory data analysis and filtering: The data count matrix was filtered for genes with a mean  
921 of less than 3 to remove very low count genes, and genes where most of the counts were zero  
922 were also removed. Model Description: A varying intercepts hierarchical modelling framework  
923 was used to model the expression for each gene. This analysis was implemented in R<sup>48</sup> and  
924 Stan<sup>49</sup>. Pathway Analysis: Gene set enrichment analysis (GSEA) was carried out using the R  
925 package GAGE, and predicted upstream regulators, canonical pathways, and diseases and  
926 functions were determined using IPA (version 01-13, Qiagen) of  $p_{adj}<0.05$  genes, excluding  
927 chemicals.

928

#### 929 hMSC attachment on 2D hydrogel surfaces

930 Human bone marrow-derived stromal cells (hMSC) were obtained from the Imperial College  
931 Healthcare Tissue Bank (ICHTB, HTA license 12275). ICHTB is supported by the National

932 Institute for Health Research (NIHR) Biomedical Research Centre based at Imperial College  
933 Healthcare NHS Trust and Imperial College London. ICHTB is approved by the UK National  
934 Research Ethics Service to release human material for research (12/WA/0196) as previously  
935 described<sup>50</sup>. The samples for this project were issued from sub-collection R16052. 50 µL 5%  
936 hydrogels formed with 5K PEG-4VS were formed in 6-well plates and 24mm Sigmacote®-  
937 treated coverslips placed on top. After hydrogel formation, 5,000 hMSC cm<sup>-2</sup> were seeded and  
938 allowed to adhere for 2h prior to the addition of basal culture media. After 24h, hMSC were fixed  
939 in 4%PFA, permeabilized in 0.2% (v/v) Triton X-100 and stained with Phalloidin-TRITC (Sigma)  
940 and DAPI. Cells were imaged on an Olympus inverted fluorescent microscope equipped with a  
941 Jenoptik Camera.

942

#### 943 Animals

944 CD45.1 mice (B6.SJL-*Ptprc<sup>a</sup>Pepc<sup>b</sup>*/BoyCrl, female, 6-8 weeks) were purchased from Charles  
945 River and *Rorc(γt)-Gfp<sup>TG</sup>* reporter mice (female, 6-10 weeks) were a kind gift from Gérard Eberl.  
946 Both animal lines were maintained at Charles River (Margate) and in the New Hunt's House  
947 King's College London animal facilities by BSU staff. Animals were maintained with enrichment  
948 in specific pathogen free conditions with a 12 light/12 dark cycle, at ~19-22°C and ~50%  
949 humidity in accordance with the UK Animals (Scientific Procedures) Act 1986 (UK Home Office  
950 Project License (PPL:70/7869 to September 2018; P9720273E from September 2018).

951

#### 952 Statistics

953 Statistical analyses were performed in GraphPad Prism version 8.1.2.

954

955

956



957 **Methods-only references**

- 958
- 959 39. Sato, T. Clevers, H. Primary mouse small intestinal epithelial cell cultures. *Methods in*  
960 *Molecular Biology* **945**, 319-28 (2013).
- 961 40. Gronke, K., Kofoed-Nielsen, M. & Diefenbach, A. in *Methods in molecular biology (Clifton,*  
962 *N.J.)* 255-265, (2017).
- 963 41. de Jong, D. H. *et al.* Improved Parameters for the Martini Coarse-Grained Protein Force  
964 Field. *Journal of Chemical Theory and Computation* **9**, 687-697 (2013).
- 965 42. Martínez, L., Andrade, R., Birgin, E. G. & Martínez, J. M. PACKMOL: A package for building  
966 initial configurations for molecular dynamics simulations. *Journal of Computational Chemistry*  
967 **30**, 2157-2164 (2009).
- 968 43. Di Marco Barros, R. *et al.* Epithelia Use Butyrophilin-like Molecules to Shape Organ-Specific  
969  $\gamma\delta$  T Cell Compartments. *Cell* **167**, 203-218.e17 (2016).
- 970 44. Lee, H., de Vries, A. H., Marrink, S. & Pastor, R. W. A Coarse-Grained Model for  
971 Polyethylene Oxide and Polyethylene Glycol: Conformation and Hydrodynamics. *The Journal of*  
972 *Physical Chemistry B* **113**, 13186-13194 (2009).
- 973 45. Plimpton, S. Fast Parallel Algorithms for Short-Range Molecular Dynamics. *Journal of*  
974 *Computational Physics* **117**, 1-19 (1995).
- 975 46. Bode, F. *et al.* Hybrid gelation processes in enzymatically gelled gelatin: impact on  
976 nanostructure, macroscopic properties and cellular response. *Soft Matter* **9**, 6986-6999 (2013).
- 977 47. Hutter, J. L. & Bechhoefer, J. Calibration of atomic force microscope tips. *Review of*  
978 *Scientific Instruments* **64**, 1868-1873 (1993).
- 979 48. Luo, W., Friedman, M. S., Shedden, K., Hankenson, K. D. & Woolf, P. J. GAGE: generally  
980 applicable gene set enrichment for pathway analysis. *BMC Bioinformatics* **10**, 161 (2009).
- 981 49. Carpenter, B. *et al.* Stan: A Probabilistic Programming Language. *Journal of Statistical*  
982 *Software* **76**, 1-32 (2017).
- 983 50. Ferreira, S. A. *et al.* Bi-directional cell-pericellular matrix interactions direct stem cell fate.  
984 *Nature communications* **9**, 4049-12 (2018).
- 985 51. Lochner, M. *et al.* In vivo equilibrium of proinflammatory IL-17+ and regulatory IL-10+  
986 Foxp3+ RORgamma t+ T cells. *The Journal of experimental medicine* **205**, 1381-93 (2008).

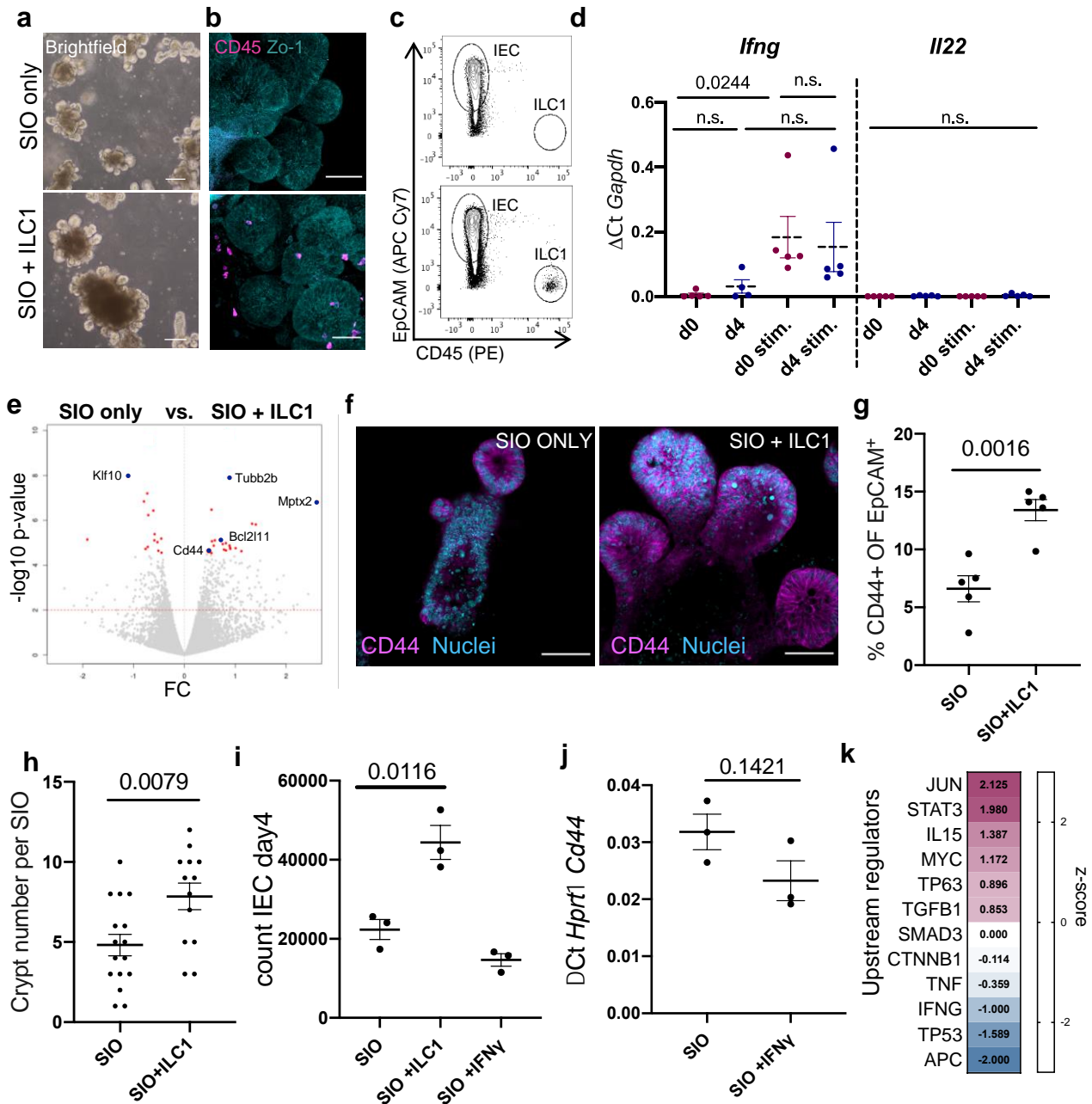


**Figure 1: ILC1 impact intestinal organoid gene expression**

a. Brightfield images, b. confocal images, and c. FACS plots of SIO cultured alone (top) or with ILC1 (bottom) (representative of experiments with ILC1 from N=3 mice) d. Expression of *Ifng* and *Il22* in ILC1 pre- (N=5 mice) and post- (ILC1 from N=4 mice) co-culture with SIO, each condition with or without 2h stimulation with 10ng/ml PMA & 1 $\mu$ M Ionomycin (stim.). e. Volcano plot ( $\log_{10}$   $p_{adj}$ -value vs. fold change) of differentially expressed genes in pico-RNAsequencing dataset, with significantly upregulated genes of interest highlighted with a blue dot (p-values calculated using the markov chain monte carlo simulation with multiple testing correction performed using the Benjamini and Hochberg (1995) method). f. Confocal images of SIO showing CD44<sup>+</sup> crypts with Lyz1<sup>+</sup> Paneth cells (Rep. of N=3). g. Flow quantification of CD44 expression in IEC (ILC1 from N=5 mice). h. quantification of crypt bud number per SIO (ILC1 derived from N=3 mice, each dot represents one organoid). i. Number of EpCAM<sup>+</sup>CD45<sup>-</sup> IEC in SIO after 4 day co-culture alone, with ILC1, or with 0.01ng/ml IFN $\gamma$  (ILC1 from N=3 mice). j. RTqPCR of IEC *Cd44* expression with or without 0.01ng/ml IFN $\gamma$  (N=3 independent experiments). k. Ingenuity pathway analysis of selected upstream regulators predicted to be driving expression signatures in ILC1 co-cultures, z-score magenta predicts high activity, blue predicts low activity. d,g,h,i,j show unpaired two-tailed t-test p-values between conditions; error bars S.E.M.; scale bars 50 $\mu$ m.

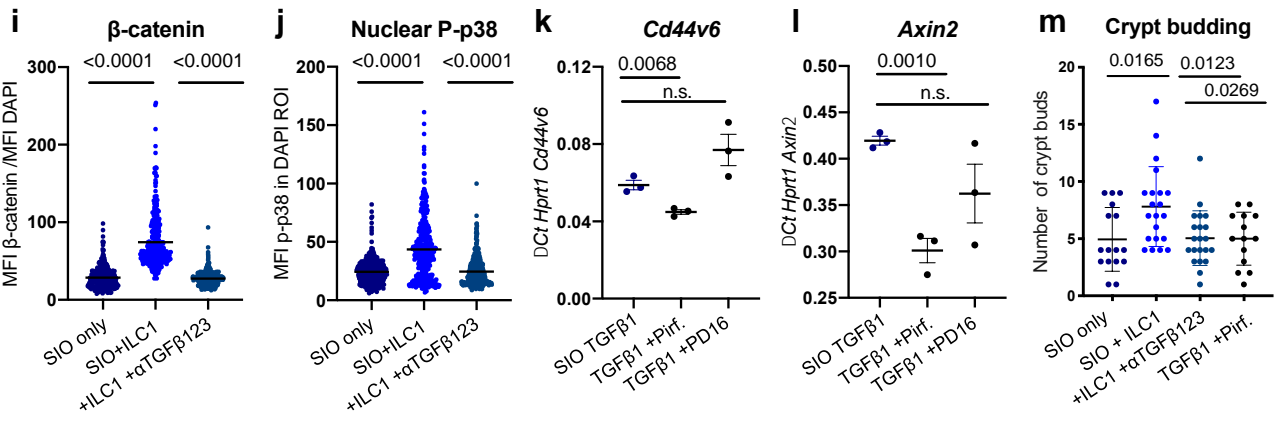
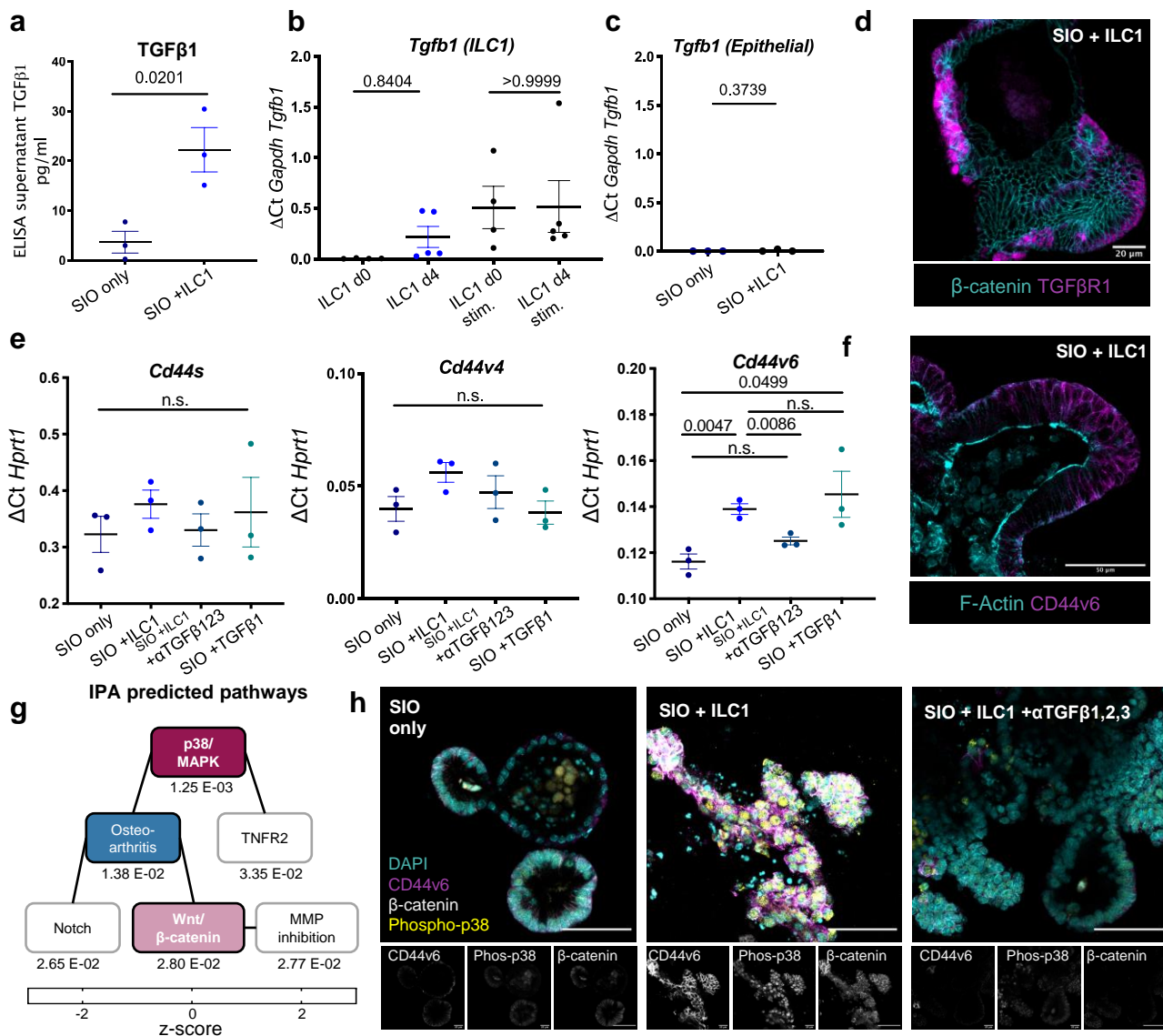


**Figure 2: ILC1 impact epithelial crypt gene expression through TGFβ1 secretion**

a. ELISA for latent and active TGFβ1 in culture supernatants on day 4 (ILC1 from N=3 mice). b. Expression of *Tgfb1* in primary murine ILC1 before (d0, N=4 mice) or after co-culture (d4, co-cultures derived from N=5 mice), with or without 2h PMA/Ionomycin activation (stim.). c. Expression of *Tgfb1* in IEC from SIO only or SIO+ILC1 on d4, (from N=3 mice, x-axis scaled to 2b). d. Localization of TGFβR1 staining in SIO co-cultured with ILC1 (d4) counterstained for β-catenin (Rep. of N=3). e. RT-qPCR with exon-specific primers for CD44 splice variants s, v4, and v6 (ILC1 derived from N=3 mice). f. Representative confocal image of CD44v6 localization in d4 SIO+ILC1, counterstained with F-Actin (Rep of N=3 mice). g. IPA of activated canonical pathways. Linked boxes contain overlapping differentially expressed genes ( $p_{adj}$  beneath boxes; magenta-midnight colouring represents high-low z-score). h. Expression patterns of CD44v6, phosphorylated p38, β-catenin and DAPI nuclei in SIO alone, with ILC1, or with ILC1 and 1ng/ml TGFβ1,2,3-neutralization (Rep of N=3 mice, scale bars 50μm). i. Quantification of phosphorylated-p38 in the DAPI<sup>+</sup> region of the experiment in (h) (experiments from N=3 mice, each dot represents one nucleus) j. Quantification of β-catenin accumulation in IEC of experiment in (h), normalized to DAPI intensity (N=3 mice, each dot represents one cell). k. *Cd44v6* expression and l. *Axin2* expression after 2day culture of SIO with TGFβ1, with TGFβ1 and Pirfenidone (5μm) or TGFβ1 and PD16 (3μm) in N=3 three separate experiments. m. Quantification of crypt budding after 4 day co-culture (OneWay ANOVA and Tukey test, each dot one SIO, quantified from three experiments with ILC1 derived from N=3 mice). a,b,c,e,k,l Two-tailed unpaired t-test, error bars show S.E.M.; i,j,m, OneWay ANOVA and Tukey test, error bars S.E.M. Scale bars indicated in overlays.

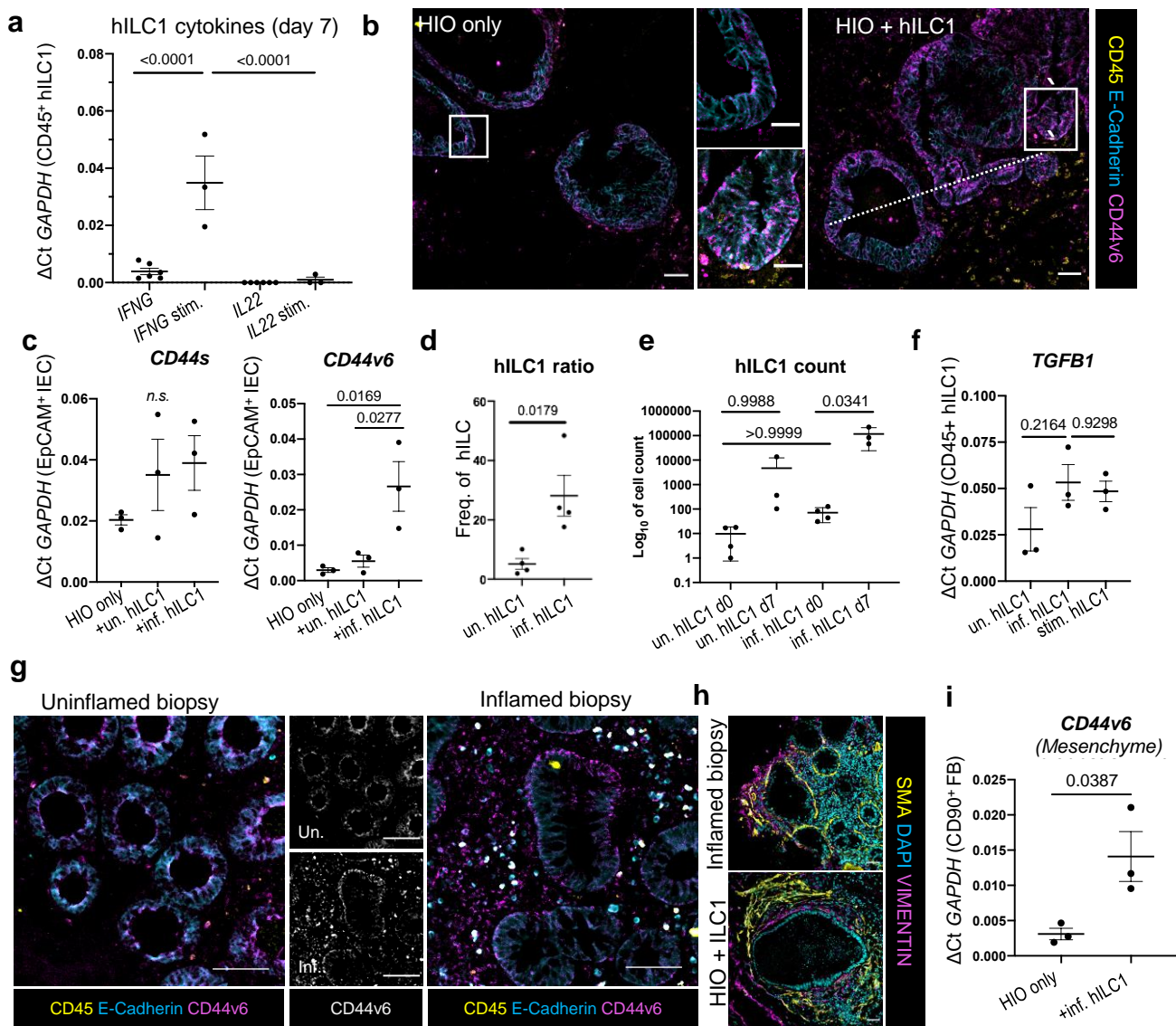


**Figure 3: Human ILC1 drive CD44v6 expression in HIO**

a. Expression of *IFNG* and *IL22* in biopsy-derived hILC1 after 7 day co-culture with HIO with (ILC1 co-cultures from N=3 patients) or without (ILC1 co-cultures from N=6 patients) 2h PMA/Ionomycin stimulation (stim.), with corresponding representative images of E-cadherin, CD44v6, and CD45 staining of HIO cultures with or without inflamed hILC1 shown in b (Scale 50 $\mu$ m), white box indicates magnified crypt (Scale 20 $\mu$ m). c. Expression of *CD44s* and *CD44v6* in FACS-purified IEC from HIO only, hILC1 co-culture, from inflamed (inf.) or uninflamed (un.) samples (N=3 patients per condition). d. Proportion of hILC1 relative to other Lineage-CD127<sup>+</sup> ILC subtypes prior to co-culture (ILC from N=4 uninflamed and N=4 inflamed tissue biopsies). e. Log<sub>10</sub> cell count of hILC1 before (d0, from N=4 patients) and after (d7, from N=3 patients) co-culture from un. and inf. biopsies. f. Relative expression of *TGFβ1* in hILC1 from N=3 inf., N=3 un., or N=3 stim. different patients after 7 day co-culture with HIO. g. Immunohistochemistry from biopsies from IBD patients with (right) or without (left) active inflammation. CD45 lymphocytes also express E-cadherin and CD44v6. h. SMA<sup>+</sup> myofibroblast and VIMENTIN<sup>+</sup> fibroblast organization around the epithelium in an inflamed patient biopsy and in HIO+ILC1 co-cultures. i. Relative expression of *CD44v6* in EpCAM<sup>-</sup>CD45<sup>-</sup>CD90<sup>+</sup> fibroblasts (FB) purified from HIO after 7 day culture with or without inflamed hILC1 (ILC1 from N=3 inflamed tissue biopsies). a,c,e,f OneWay ANOVA with Tukey's test, error bars S.E.M; d,i, unpaired two-tailed t-test, error bars S.E.M.. Scale bars 50 $\mu$ m.



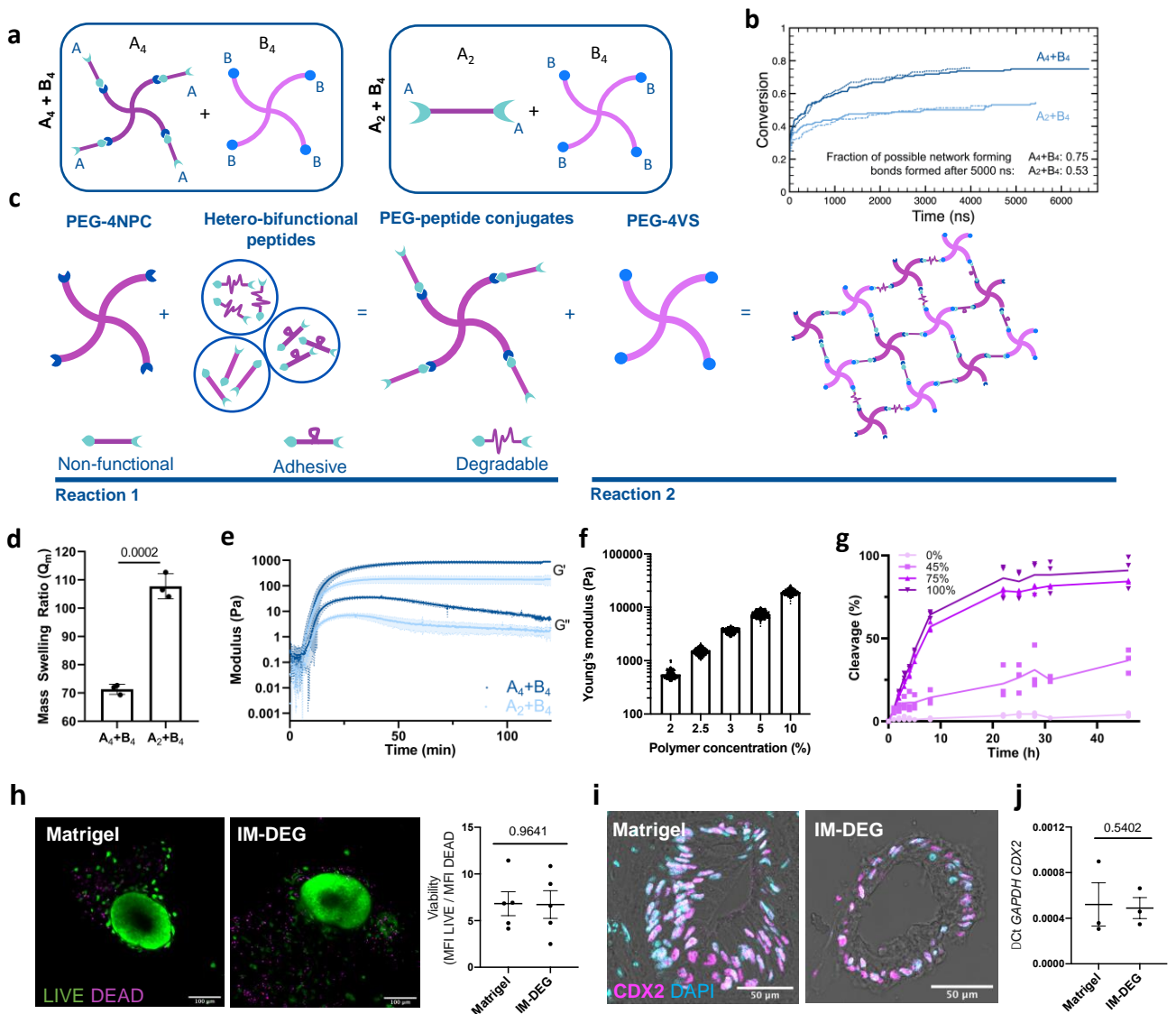


**Figure 4: Modular PEG-based hydrogels form at low polymer concentrations and support HIO viability and phenotype**

a. Molecular dynamics simulations of hydrogel cross-linking using either an  $A_4+B_4$  or  $A_2+B_4$  design. b. Plot showing fraction of total possible network-forming cross-links formed in the molecular dynamics simulations. Lines show replicate simulations per condition. c.  $A_4+B_4$  hydrogels are formed using two sequential and orthogonal click reactions. PEG-4NPC is first conjugated with degradable, adhesive, or non-adhesive/non-degradable peptides, and then reacted 1:1 with PEG-4VS. Stiffness is altered by changing polymer concentration. Ligand density/degradability are controlled by varying the percent of their respective conjugates. d. Mass swelling ratio for hydrogels formed using either  $A_4+B_4$  or  $A_2+B_4$  designs (N=3 independent hydrogels, error bars S.D.). e. Rheological measurements of hydrogel formation. Plots show means and standard deviations (shading) of  $G'$  and  $G''$  obtained using time sweeps (N=3 independent hydrogels). f. Young's modulus (Pa) of hydrogels as determined by atomic force microscopy-based indentation measurements (N=3 independent hydrogels). g. Percent cross-linking peptides cleaved over time in the presence of MMP9 for hydrogels formed with varying percentages of degradable peptide. Lines connect mean values (N=3 independent hydrogels). h. Representative images and quantification of HIO viability after 7-day encapsulation in Matrigel or IM-DEG (N=3 encapsulation experiments, unpaired student t-test, error bars S.E.M.). i. Representative images of HIO after 7-day culture in Matrigel or IM-DEG show nuclear CDX2 localization in the epithelial monolayer, representative of N=3 encapsulation experiments, quantified in j., showing relative expression of hindgut marker *CDX2* in d75 whole HIO in Matrigel (MG) or after 7-day encapsulation in IM-DEG (N=3 encapsulation experiments, Two-tailed, unpaired t-test, error bars S.E.M.). Scale bars 50 $\mu$ m.

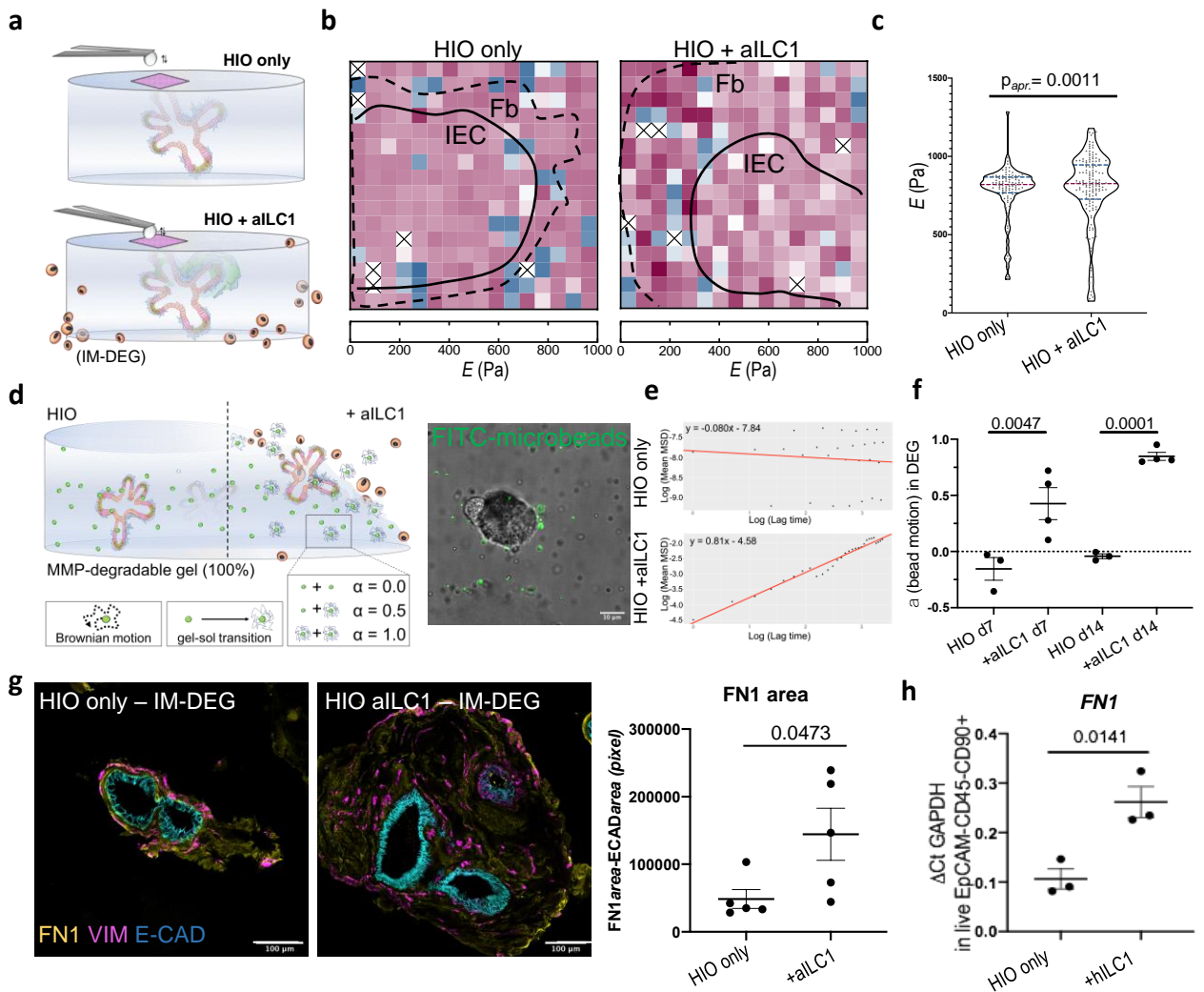


**Figure 5: Ancillary ILC1 drive HIO matrix remodelling in synthetic hydrogels**

a. Schematic of AFM-based stiffness mapping strategy of HIO in IM-DEG gels, wherein the gel content (HIO) remains constant for measurement, as ancillary hILC1 from inflamed patient tissues surround the gel. b. Representative  $150\mu\text{m} \times 150\mu\text{m}$  stiffness maps (Pa) of HIO-laden IM-DEG gel without (left) or with (right) aILC1, showing approximate outline of epithelial layer (Ep) and surrounding fibroblast region (Fb) based on brightfield images (Supplementary Fig. 26). White/x squares denote omitted measurements that failed to meet QC standards, Median  $E_{\text{HIO}}=790.9$ , Median  $E_{\text{HIO+aILC1}}=779.9$ . c. Violin plots summarize measurements of Young's modulus ( $E$ , Pa) on HIO-laden IM-DEG gels measured directly above organoids with or without aILC1 (Approximate  $p=0.0011$ ,  $D=0.2525$ ; non-parametric Kolomogorov-Smirnov test,  $N=3$  force maps per condition, each dot represents one force curve). d. Schematic of microrheology strategy, with corresponding sample confocal image showing distribution of fiducial FITC within an HIO-laden, fully degradable gel (scale bar  $10\mu\text{m}$ , representative of  $N=4$  encapsulation experiments).  $\alpha$  is an indicator of bead motion ( $1$ =Brownian motion,  $0$ =immobile,  $\alpha$  transitions from  $0$  to  $1$  as the local hydrogel undergoes a gel-sol transition). e. Representative plots generated in R showing the logarithmic slope of the mean-squared displacement of beads. f.  $\alpha$  for HIO encapsulated in 100% DEG gels after 7 and 14 days with or without aILC1 ( $N=4$  encapsulation experiments). g. Representative staining of Fibronectin1 deposition and Vimentin+ fibroblasts in HIO with or without aILC1 (max projection 10 z-stacks) with quantification of FN1+ area normalized to ECAD+ area ( $N=5$  separate organoid areas). h. Expression of *FN1* in EpCAM-CD45-CD90+ FB after 7 day culture with or without inflamed hILC1 (ILC1 derived from  $N=3$  patients). f,g, unpaired two-tailed student t-test, h. OneWay ANOVA with Tukey's test; Error bars S.E.M; scale bars  $100\mu\text{m}$ .

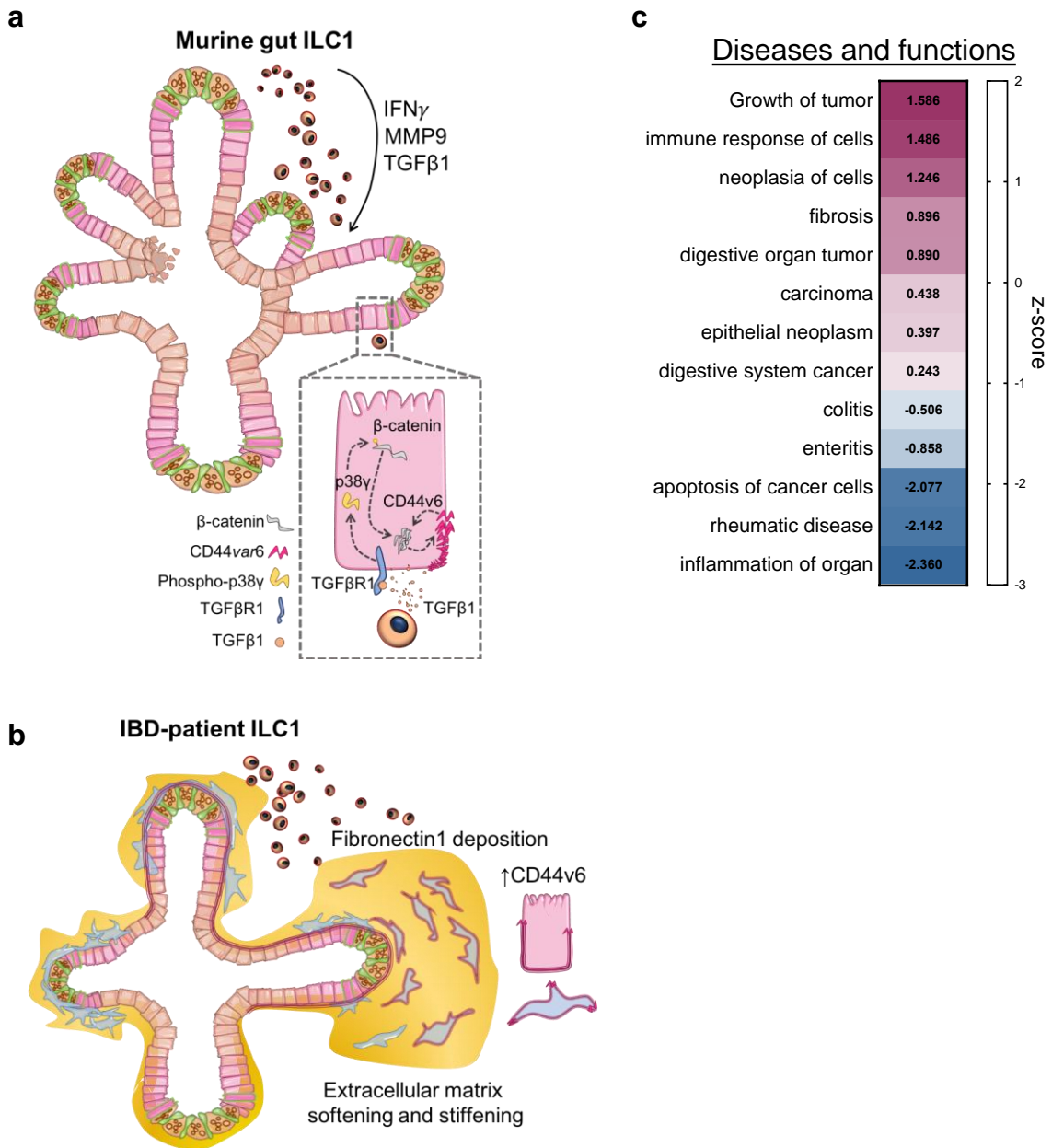


**Figure 6: Overview of proposed impact of ILC1 on gut organoids**

a. Murine ILC1 drive epithelial crypt budding in small intestine organoids through TGF $\beta$ 1-induced phosphorylation of p38 $\gamma$ , which drives  $\beta$ -catenin accumulation and expression of *Axin2* and *CD44v6*. We propose that CD44v6 and  $\beta$ -catenin might engage in a positive feedback loop, driving epithelial subtype-non-specific proliferation. b. hILC1 derived from IBD patients express *TGFBI* and *MMP9*. ILC1 isolated from tissues with active inflammation also drive expression of both epithelial and mesenchymal CD44v6 in HIO. Moreover, these patient-derived ILC1 drive increased deposition of Fibronectin1 and MMP-mediated matrix degradation, resulting in a balance of matrix softening and stiffening. c. IPA of the murine RNA-sequencing dataset showing cumulative gene enrichment (z-score) in SIO co-cultured with ILC1 indicative of activation (magenta) and inhibition (blue) of selected gastrointestinal and inflammatory diseases and function (ILC1 derived from N=3 mice).